processes

MDPI

Article

A Comprehensive Study of Machine Learning for Waste-to-Energy Process Modeling and Optimization

Jianzhao Zhou [1], Jingyuan Liu [1], Jingzheng Ren [1,2,*] and Chang He [3]

[1] Research Institute for Advanced Manufacturing, Department of Industrial and Systems Engineering, The Hong Kong Polytechnic University, Hong Kong SAR, China
[2] Research Center for Resources Engineering Towards Carbon Neutrality, The Hong Kong Polytechnic University, Hong Kong SAR, China
[3] School of Chemical Engineering and Technology, Sun Yat-Sen University, Zhuhai 519082, China
* Correspondence: jzhren@polyu.edu.hk

Abstract

This study presents a comprehensive study integrating machine learning, life cycle assessment (LCA) and heuristic optimization to achieve a low-carbon medical waste (MW)-to fuel process. A detailed process simulation coupled with cradle to gate LCA is employed to generate a dataset covering diverse process operation conditions, embodied carbon of supplying H_2 and the associated carbon emission factor of MW treatment (CEF). Four machine learning techniques, including support vector machine, artificial neural network, Gaussian process regression, and XGBoost, are trained, each achieving test R^2 close to 0.90 and RMSE of ~0.26. These models are integrated with heuristic algorithms to optimize operating parameters under various green hydrogen mixes (20–80%). Our results show that machine learning models outperform the detailed process model (DPM), achieving a minimum CEF of ~1.3 to ~1.1 kg CO_2-eq/kg MW with higher computational stabilities. Importantly, the optimization times dropped from hours (DPM) to seconds (machine learning models) and the combination of Gaussian process regression and particle swarm optimization is highlighted, with an optimization time under one second. The optimized process holds promise in carbon reduction compared to traditional MW disposal methods. These findings show machine learning can achieve high predictive accuracy while dramatically enhancing optimization speed and stability, providing a scalable framework for extensive scenario analysis during waste-to-energy process design and further real-time optimization application.

Keywords: waste-to-energy; machine learning; life cycle assessment; process modeling and optimization

Academic Editor: Marco Vaccari

Received: 17 July 2025
Revised: 20 August 2025
Accepted: 22 August 2025
Published: 24 August 2025

Citation: Zhou, J.; Liu, J.; Ren, J.; He, C. A Comprehensive Study of Machine Learning for Waste-to-Energy Process Modeling and Optimization. *Processes* **2025**, *13*, 2691. https://doi.org/10.3390/pr13092691

1. Introduction

Medical waste (MW) refers to waste materials generated during the diagnosis, treatment, or immunization of humans and animals [1]. Due to pandemics, the annual global production of related MW has climbed sharply, arriving at more than 2.9 million tonnes in 2022 alone [2]. Different from typical waste types, approximately 15% of MW is categorized by high toxicity, corrosivity, or pathogenicity [3]. Therefore, a rapid increase in MW presents both societal and environmental challenges, necessitating more urgent handling and disposal.

To date, most MW streams are first collected and sterilized, then either landfilled or incinerated [4,5]. Landfilling, while widely practiced, occupies extensive land, generates

methane, and produces leachate that can contaminate soil and groundwater [6,7]. Incineration can effectively reduce waste volume and harnesses energy from thermal oxidation, but it also leads to significant emission of greenhouse gases (GHGs) and hazardous by-products (e.g., dioxins, furans) [8]. To mitigate the impact from MW treatment, policymakers and engineers worldwide are exploring more sustainable strategies. For example, the European Union is progressively reducing landfilling and incineration reliance by promoting adoption of green technologies and improving waste management regulations [9]. Likewise, Hong Kong's Climate Action Plan 2050 prioritizes waste reduction and the expansion of waste-to-energy infrastructure [10]. Waste-to-energy conversion not only helps recover the energy content contained in waste but also offers economic benefits and opportunities for GHG mitigation.

Quite a few thermochemical methods have been investigated to recover energy from MW (mainly including incineration, pyrolysis, and gasification) since high energy output could be achieved compared to biochemical-based methods [11]. For instance, Chaiyat [12] developed a system integrating infectious medical waste incinerator with an organic Rankine cycle for power generation, reporting an energy efficiency of 0.91% and an exergy efficiency of 0.89%. It was also shown that waste-incineration-based fly ash can be used for preparing filling material [13]. In another study, Zhao et al. designed a pyrolysis-based process for disposable respirator treatment, achieving an internal rate of return of 21.5% and a seven-year payback [14]. To curb pollutant emissions inherent in incineration and pyrolysis, gasification has garnered attention as an attractive alternative [15]. Under oxygen-limited gasifying conditions, organic matters are converted into syngas mainly containing CO and H_2, which can be tailored for diverse downstream products. In this way, subsequent purification like pressure swing adsorption (PSA) can be used for high-purity H_2 production. And it was shown that H_2 production through waste mask gasification held levelized emissions as low as 1.27 kg CO_2-eq per kg treated waste [16]. Alternatively, the raw syngas can be catalytically upgraded into fuels and chemicals such as methanol [17] and dimethyl ether [18], contributing to flexible uses and economic value. An additional and practical source of uncertainty for MW-to-fuel systems is the carbon intensity and availability of hydrogen used for downstream upgrading or CO_2 utilization, which should be explicitly considered when designing low-carbon waste-to-energy pathways.

Although process simulations based on thermodynamics and kinetics have been widely used in waste-to-energy design and assessment [19,20], these models are usually complex and coupled with numerous nonlinear algebraic and differential equations, thus posing computational challenges in further process understanding and optimization [18]. This has motivated the exploration of data-driven surrogate models, which can approximate the behavior of these complex systems with far lower computational cost.

In recent years, machine learning approaches have revolutionized the modeling of waste-to-energy systems. Table 1 outlines recent studies on process modeling and optimization. Various machine learning techniques have been used. For example, Zhu et al. [21] applied random forest to predict the yield and carbon contents of biochar derived from biomass pyrolysis, with an R^2 of nearly 0.85. Furthermore, Tang et al. [22] explored feature reduction in a support vector machine (SVM) and random forest, and the results showed that six features covering pyrolysis conditions and biomass properties were sufficient to accurately predict the pyrolytic gas yield with an RMSE of less than 5.7%. In another study, both gradient-boosted regression trees and artificial neural network (ANN) were trained to forecast syngas composition from waste gasification, reporting excellent predictive performance, and then the prediction models were integrated in process assessment with Aspen Plus [23]. Similarly, various machine learning models including random forest, SVM, MLP and gradient boosting have been used in wet organic waste gasification, with an R^2 of >0.9

for each prediction achieved [24]. Although these proposed machine learning models have shown high accuracy in modeling waste-to-energy process, detailed and comprehensive study on revealing various machine learning's performance across both surrogate-modeling accuracy and optimization efficiency, especially in MW-to-fuel applications, is still lacking, as presented in Table 1. Typically, real-time process optimization demands models that can be evaluated and optimized rapidly. Prior work in chemical process control has underscored the need for both precise prediction and efficient optimization [25,26]. In addition, early-stage process design accounts for numerous external uncertainties, often necessitating thousands of simulations for evaluation and comparison. Thus, efficient process optimization is important to enable thorough uncertainty analysis within practical time frames. Zhou et al. [16] have shown Gaussian process regression (GPR) is excellent in surrogating detailed gasification process models, markedly accelerating operation optimization to roughly four seconds per run. Despite these individual advances, systematic studies that benchmark diverse ML techniques are still underexplored. In particular, comprehensive head-to-head comparisons of how different algorithms perform when embedded within optimization are notably absent, yet critical for guiding future choices of machine learning in sustainable MW-to-energy process design.

Table 1. Evaluation results of different models.

Models	RMSE	MAE	MRE
LR	0.2781	0.1826	0.0796
SVM	0.2609	0.1467	0.0617
ANN	0.2581	0.1599	0.0700
GPR	0.2548	0.1540	0.0689
XGBoost	0.2669	0.1646	0.0710

To address the above-mentioned limitations of existing machine-learning-based work on MW-to-energy systems, this study first establishes a conceptual process for converting MW into Fischer–Tropsch (FT) liquid fuels and evaluates its carbon footprint given the recent high concerns on carbon emission [27]. Then, a dataset of life-cycle emissions under varied operating and environmental conditions through high-fidelity simulation is generated. Four widely recognized machine learning techniques, including SVM, ANN, GPR, and extreme gradient boosting (XGBoost), are trained to construct computationally concise surrogate models. Finally, each surrogate is embedded within an optimization framework to rapidly identify optimal operating conditions, demonstrating how different ML approaches influence both the speed and the quality of process design. The main contributions of this study are as follows:

(1) Developing and comparing four distinct machine learning models to predict environmental performance of a promising MW-to-FT process, providing clear guidance on their relative accuracy and generalizability.
(2) Coupling each surrogate with different optimization algorithms to reveal model performance in the efficiency and robustness of process optimization, highlighting the importance of effective optimization in unlocking waste-to-energy process's potential.

Overall, our systematic evaluation of machine-learning-driven modeling and optimization strategies offers a practical roadmap for selecting and deploying these AI tools in the design of next-generation waste-to-energy systems.

2. Methodology

This study develops and compares machine learning models to predict and optimize the life cycle environmental performance of a MW-to-FT fuel process, as outlined in Figure 1.

First, a detailed process model is developed by using the Aspen Plus simulation platform and its environmental impact is quantified via life cycle assessment (LCA), yielding a carbon emission factor of MW treatment (CEF) for each set of operating conditions and embodied carbon emissions of consumable materials. Second, a dataset is generated by systematically varying key operating parameters (e.g., reactor temperatures, embodied carbon of input materials), with each case providing simulation outputs and corresponding LCA results. Next, four distinct surrogate models (SVM, ANN, GPR and XGBoost) are trained to surrogate the high-fidelity simulation with low computational expense. Finally, each surrogate is integrated with heuristic optimization algorithms to identify operating conditions that minimize the CEF under multiple hydrogen-supply scenarios. All simulations and ML workflows are executed on a Windows 10 PC equipped with an AMD Ryzen 7 5800H (6 cores, 3.2 GHz) and 16 GB RAM.

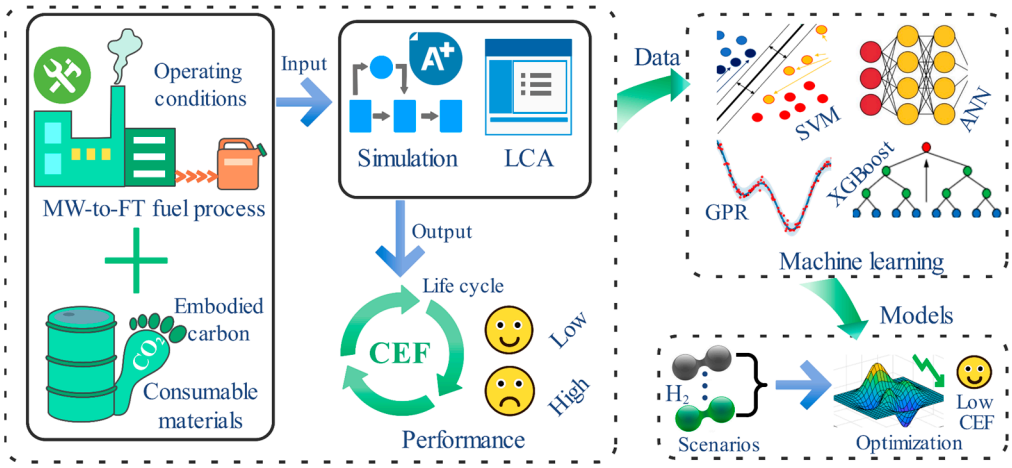

Figure 1. Workflow of this study.

2.1. Process Development

A comprehensive process incorporating plasma gasification, carbon capture, FT synthesis and combined heat and power generation is designed to convert MW into FT fuel, as shown in Figure 2. Plasma gasification is widely regarded as one of the most effective technologies for treating hazardous medical waste [28]. The extremely high operating temperatures (often reaching several thousand °C) achieved in plasma gasifiers are sufficient to completely destroy pathogens and organic contaminants, thereby eliminating the need for additional disinfection pretreatment [29]. In this study, a typical waste surgical mask was used as the feedstock for analysis and the proximate and ultimate analysis results of this MW sample is listed in Table A1, reflecting the sample's chemical composition.

The detailed process model (DPM) was then developed in a well-established process simulation platform, Aspen Plus, which has been widely used in waste-to-energy process design and assessment previously [19,20], demonstrating high feasibility to inform decision-making. For non-conventional components like MW, the HCOALGEN and DCOALIGT models were used to estimate the enthalpy and density [30]. For the conventional components, the Peng–Robinson/Boston–Mathias (PR-BM) equation of state was employed to estimate their thermodynamic parameters [31].

The gasification process comprises three zones, drying, pyrolysis and gasification, which are simulated by the "RStoic" model, the "RStoic" model and the "RGibbs" model, respectively [18]. As the primary unit within the process, the used gasification model has been validated in previous studies by using experimental data [32]. Here, pure oxygen and water are used as gasifying agents, following previous studies [16]. The inert and dense residue is removed from the bottom of gasifier, while the derived syngas is cooled and sent

to a reactor for reverse water gas shift (RWGS) reaction ($H_2 + CO_2 \rightarrow CO + H_2$) at 600 and 24.5 bar [33]. With supplemental H_2 makeup, the upgraded syngas enters a two-stage FT synthesis unit (modeled by the "RStoic" model) to produce FT fuel, including naphtha, jet fuel, diesel and wax. The configuration of FT reactors can be found in our previous studies in detail [32]. The product distribution of FT synthesis is based on the widely accepted Anderson–Schulz–Flory distribution [34]. After separating the produced fuels (fractioned by carbon chain length [35]) via distillation, the remaining gases containing unreacted syngas and light hydrocarbon (C1–C4) are split: a portion is recycled back to the FT reactors, while the balance is directed to a PSA unit for H_2 recovery. The captured H_2 is returned to the RWGS step, and the PSA off-gas is used to drive a combined heat and power generation unit including fuel gas combustion and a steam cycle for power generation. To mitigate carbon emissions, both pre-combustion and post-combustion carbon capture are incorporated into the process through an monoethanolamine (MEA) scrubber (widely-used capture efficiency of 85% [36] and energy duty of 4 MJ per kg captured CO_2 [37]), with the recovered CO_2 looped back to the RWGS reactor. Waste heat from exothermic units is recovered for steam generation to enhance overall efficiency [16]. The key operating parameters involved in the process are outlined in Table A2 and the simulation results of a representative base case (where decision variables are fixed at the midpoint of their studied ranges) are presented in Table A3. The main assumptions in modeling include steady-state operation, no losses in piping, and complete tar conversion in the gasifier [16,38].

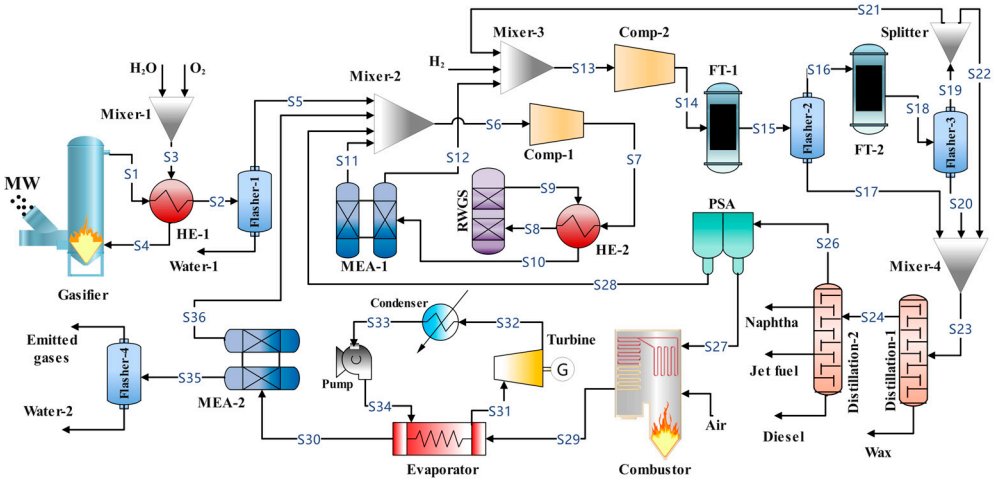

Figure 2. Flowsheet of MW-to-FT fuel system.

2.2. Life Cycle Assessment

To evaluate the carbon footprint of the proposed MW-to-FT fuel system, a cradle-to-gate LCA is employed to calculate the CEF, reflecting the equivalent CO_2 emission level per unit medical waste processed. The LCA boundary (see Figure 3) covers five core process stages: plasma gasification, syngas purification, FT synthesis, combined heat and power generation, and flue gas treatment. Emissions are classified into three categories: (1) on-site direct emission during process operation; (2) indirect emission associated with upstream production of consumable materials (e.g., catalysts, sorbents, process water); and (3) indirect emission from the generation of utilities (e.g., steam, cooling water, and electricity). Notably, following previous similar studies [14], the sorting and collection of waste are excluded from the system boundary in this study. Life cycle inventory data is sourced from the Ecoinvent database [39], and all GHG impacts are characterized using the IPCC 2013 climate change methodology [40]. To account for credit-worthy energy

outputs including FT fuels, turbine electricity, and recovered heat, the avoided emissions are subtracted from the total. Thus, the overall CEF is calculated as in Equation (1).

$$CEF = NCE/m_{MW} \quad (1)$$

where m_{MW} is the mass flowrate of processing MW and NCE is the net carbon emission, including the direct emission (DE), indirect emission due to raw material acquisition (IE_m) and utility generation (IE_u), as well as the avoided emission (AE) from products, as calculated by Equation (2).

$$TCE = DE + IE_m + IE_u - AE \quad (2)$$

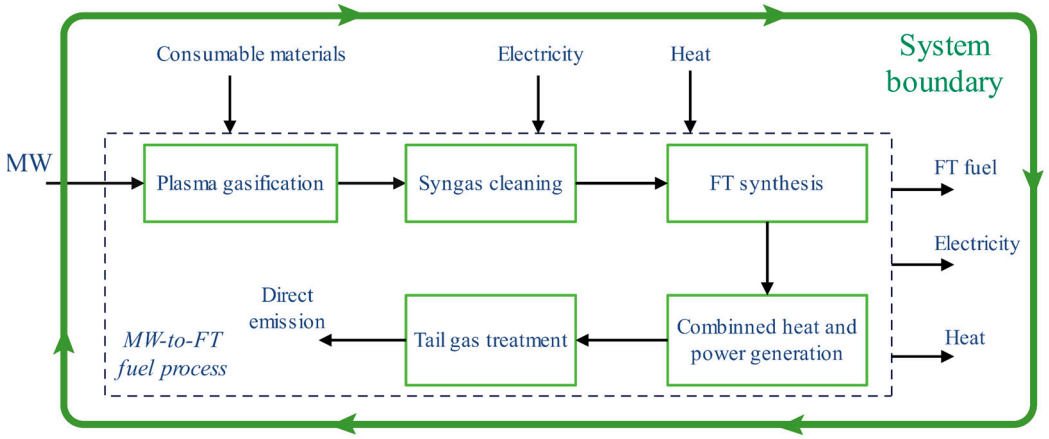

Figure 3. System boundary of life cycle assessment.

2.3. Data Collection

Data is collected by performing detailed process simulation and LCA calculation. Through system analysis, five input features that most strongly influence the cradle-to-gate CEF are determined: gasifier temperature (GT), equivalence ratio (ER), steam-to-waste ratio (SWR), splitting ratio of light gases to the PSA unit (SRLG), and the levelized carbon emission of makeup H_2 (LCEH). LCEH reflects market-driven variations in H_2 sourcing (e.g., green, blue, or grey H_2) and directly affects the overall emissions of the designed process, making it a critical factor. The ranges of these variables are summarized in Table A2, with GT, ER, SWR selected based on prior literature, SRLG determined from 0 to 1, and LCEH bounded by the emissions associated with photovoltaic (PV) electrolysis and steam methane reforming (SMR) [16]. Within these bounds, random sampling is employed to generate diverse scenarios, and each sampled point is evaluated through process simulation and LCA to produce a corresponding CEF. To approximate the real-world measurement and modeling uncertainty, Gaussian noise (5% standard deviation) is introduced on the collected data to test the performances of various machine learning algorithms under realistic data variability [41].

2.4. Machine Learning Techniques

Four representative supervised learning techniques were selected for surrogate model development, including SVM, ANN, GPR and XGBoost, covering connectionist, kernel-based, probabilistic, and ensemble learning paradigms, respectively. SVMs leverage the kernel trick to learn nonlinear decision functions from relatively small datasets [42] while providing strong regularization against overfitting. ANNs are highly flexible function approximators that capture complex, high-dimensional nonlinear mappings and interactions. GPR offers a probabilistic surrogate that provides principled predictive uncertainty

(predictive mean and variance), which is useful for uncertainty-aware optimization and for guiding further sampling. XGBoost is a tree-based ensemble that excels on tabular data, often achieving strong predictive performance with fast training, built-in regularization, and interpretable feature-importance measures. By using these models, the strengths and trade-offs across approaches commonly used for complex process systems can be evaluated. All models are developed in the MATLAB 2021a platform. Below, the mathematics of these machine learning methods and the used evaluation metrics are briefly summarized.

2.4.1. Support Vector Machine (SVM)

SVM is a machine learning technique that is particularly well suited for tasks with limited training data [42] and has been successfully used in solving regression problems such as yield forecasting [43] and material property estimation [44]. The goal of SVM regression is to determine a function $f(x)$ that maps input vectors $x_i \in \mathbb{R}^d$ to the targeted output $y \in \mathbb{R}$ by fitting a hyperplane in feature space. This hyperplane is determined by minimizing prediction error while maximizing the margin, i.e., the distance between the plane and the closest data points [45].

In linear SVM regression, $f(x)$ is formulated as Equation (3), determined by solving an optimization problem that balances margin width against regression loss [46].

$$f(x_j) = \sum_{S.V.} (\alpha_i - \alpha_i^*) \times (x_i \cdot x_j) + b \tag{3}$$

where α_i, α_i^* (the introduced nonnegative multipliers) and b are the parameters to determine the optimal hyperplane, which can be obtained by training. $(x_i \cdot x_j)$ denotes the dot product of the input vectors x_i and x_j. Here, the support vectors $(x_i,\ y_i)$ are those training samples corresponding to nonzero coefficients α_i or α_i^*. Thus, the prediction is completely determined by the support vectors.

In nonlinear SVM regression, the input vectors are projected into a high-dimensional space via a kernel function $K(x_i,\ x_j)$, which can effectively separate the data points and capture complex relationships. The resulting regression function is then expressed in terms of support vectors and the chosen kernel, as given in Equation (4) [42].

$$f(x_j) = \sum_{S.V.} (\alpha_i - \alpha_i^*) K(x_i,\ x_j) + b \tag{4}$$

Typical nonlinear kernel function includes polynomial and Gaussian kernels as calculated by Equations (5) and (6) [42,47].

$$K_{polynomial}(x_i,\ x_j) = (1 + x_i \cdot x_j)^d \tag{5}$$

$$K_{Gaussian}(x_i,\ x_j) = exp\left(-\|x_i - x_j\|^2\right) \tag{6}$$

where d is the degree of polynomial expression; second degree (polynomial2) or third degree (polynomial3) are usually selected.

2.4.2. Artificial Neural Network (ANN)

An ANN typically consists of an ordered sequence of layers, an input layer, one or more hidden layers, and an output layer, where each layer k contains a set of neurons whose outputs depend on the previous layer's activations. Between layer $k-1$ and k, each neuron j computes a weighted sum of its inputs plus a bias and is then activated by a nonlinear function. Formally, the value of neuron j in layer k ($H_{j,k}$) is calculated by Equation (7) [48].

$$H_{j,k} = f\left(\sum_{i=1}^{n} \omega_{i,j,k} x_{i,k-1} + b_{j,k}\right) \tag{7}$$

where $\omega_{i,j,k}$ is the weight connecting i-th neuron in $k-1$-th layer and j-th node in k-th layer, $b_{j,k}$ is the bias term for j-th neuron in k-th layer, and n is the number of neurons in $k-1$ layer. f is the activation function that introduces nonlinearity. In this work, a Rectified Linear Unit (*ReLU*), as shown in Equation (8), is employed due to its ability in modeling chemical systems [49].

$$ReLU(x) = max(x, 0) \tag{8}$$

2.4.3. Gaussian Process Regression (GPR)

A Gaussian process defines a distribution over functions such that any finite collection of function values has a joint Gaussian distribution. In regression settings, one places a Gaussian process prior on the unknown function, as expressed by Equation (9) [50].

$$f(x) \sim GP\big(m(x), k\big(x, x'\big)\big) \tag{9}$$

where the mean function $m(x)$ represents the expected output at a given input x (Equation (10)) and $k(x, x')$ is a co-variance function, reflecting how the dependence between the function values at different inputs x and x' co-varies (Equation (11)) [50].

$$m(x) = E[f(x)] \tag{10}$$

$$k\big(x, x'\big) = E\big[\big(f(x) - m(x)\big)\big(f\big(x'\big) - m\big(x'\big)\big)\big] \tag{11}$$

where k is commonly called the kernel function of Gaussian process. To achieve various fitting tasks, different kernel functions have been proposed and developed, mainly including radial basic function (RBF) kernel, Matern 3/2 kernel, rational quadratic (RQ) kernel and automatic relevance determination squared exponential (ARDSE) kernel, as calculated by Equations (12)–(15) [51–53], respectively.

$$k\big(x, x'\big) = \sigma_f^2 exp\left(-\frac{r}{2\sigma_l^2}\right) \tag{12}$$

$$k\big(x, x'\big) = \sigma_f^2\left(1 + \frac{\sqrt{5}r}{\sigma_l} + \frac{5r^2}{3\sigma_l^2}\right)exp\left(-\frac{\sqrt{5}r}{\sigma_l}\right) \tag{13}$$

$$k\big(x, x'\big) = \sigma_f^2\left(1 + \frac{r^2}{2\alpha\sigma_l^2}\right)^{-\alpha} \tag{14}$$

$$k\big(x, x'|\theta\big) = \sigma_f^2 exp\left[-\frac{1}{2}\sum_{m=1}^{d}\frac{\left(x_m - x'_m\right)^2}{\sigma_m^2}\right] \tag{15}$$

where σ_f is the signal standard deviation, and σ_l is the characteristic length scale. r is the Euclidean distance between x and x', as calculated by Equation (16). α is a positive-valued scale-mixture parameter and θ is a parameterization vector. σ_m is a separate length scale for each predictor m ($m = 1, 2, \ldots, d$).

$$r = \sqrt{(x - x')^T(x - x')} \tag{16}$$

In regression, the prior distribution of outputs (y) can be expressed by Equation (17) [16].

$$y \sim N\Big(0, k\big(x, x'\big) + \sigma_n^2 I_n\Big) \tag{17}$$

where N denotes the multivariate normal distribution. σ_n is the variance in the observation noise. I_n is an $n \times n$ identity matrix. Assuming the joint distribution over the testing set

x' and training set x, the combined vector of observed outputs y and predicted outputs y' follows [54]:

$$\begin{bmatrix} y \\ y' \end{bmatrix} = N\left(0, \begin{bmatrix} k(x,x) + \sigma_n^2 I_n & k(x,x') \\ k(x,x')^T & k(x',x') \end{bmatrix}\right) \tag{18}$$

2.4.4. Extreme Gradient Boosting (XGBoost)

XGBoost is an emerging machine learning algorithm proposed in 2016 [55]. Based on a gradient boosting framework, the model's prediction for sample i is the sum of the outputs from K individual weak learners (decision trees), as shown in Equation (19) [56].

$$\hat{y}_i = \sum_{k=1}^{K} f_k(x_i) \tag{19}$$

where $f_k(x_i)$ represents the prediction of learner k for sample i. The performance is influenced by the tree's structure, like the maximum depth of tree [57]. During training, XGBoost sequentially adds new trees to correct the errors of the existing ensemble, optimizing an objective that combines a differentiable loss function ζ, as shown in Equation (20) [58].

$$\zeta = \sum_i l(y_i, \hat{y}_i) + \sum_k \Omega(f_k) \tag{20}$$

where $l(y_i, \hat{y}_i)$ is the loss function, which is determined by the actual value y_i and predicted value $\hat{y}_i$ and mean squared error is one of the most frequently used regression loss function [56]. $\Omega(f_k)$ represents the complexity of k-th tree, which is a penalty function used to prevent overfitting. At iteration t, the prediction is updated as Equation (21) [59].

$$\hat{y}_i = \hat{y}_i^{t-1} + f_t(x_i) \tag{21}$$

where $\hat{y}_i^{t-1}$ is the prediction of the t-th iteration and thus the loss function in t-th iteration ζ^t is expressed as in Equation (22) [58].

$$\zeta^t = \sum_i l\left(y_i, \hat{y}_i^{t-1} + f_t(x_i)\right) + \sum_k \Omega(f_k) \tag{22}$$

The corresponding objective ζ^t is approximated using a second-order Taylor expansion for efficient computation [58]. Key strengths of XGBoost include built-in regularization to reduce overfitting, robust handling of missing values, and parallelized tree construction, making it both accurate and scalable in different tasks [60].

2.4.5. Evaluation Metrics

To comprehensively evaluate the developed machine learning models, several metrics, including the coefficient of determination (R^2), the root mean square error ($RMSE$), mean absolute error (MAE) and mean relative error (MRE), are used in this work, as calculated by Equations (23)–(26) [49,61], respectively.

$$R^2 = 1 - \frac{\sum_{i=1}^{n}(y_i - \hat{y}_i)^2}{\sum_{i=1}^{n}(y_i - \overline{y_i})^2} \tag{23}$$

$$RMSE = \sqrt{\frac{1}{n}\sum_{i=1}^{n}(y_i - \hat{y}_i)^2} \tag{24}$$

$$MAE = \frac{1}{n}\sum_{i=1}^{n}|y_i - \hat{y}_i| \tag{25}$$

$$MRE = \frac{1}{n}\sum_{i=1}^{n}\left|\frac{y_i - \hat{y}_i}{y_i}\right| \tag{26}$$

2.5. Process Optimization

This study aims to determine the best operating parameters for the minimum CEF of the developed process with the constraint of market LECH. The optimization problem can be formulated as in Equation (27).

$$s.t. \begin{cases} Min\ CEF = f(o_i, LECH) \\ LECH = LECH_j,\ j = 1, 2, 3 \ldots n \\ o_i^{min} \le o_i \le o_i^{max} \end{cases} \quad (27)$$

where o_i is the i-th operating condition, f is the mapping function, $LECH_j$ represents the $LECH$ under j-th scenario, and o_i^{min} and o_i^{max} are the lower and upper bounds of o_i, respectively.

To compare surrogate-based optimization with the high-fidelity process model, this study defines four hydrogen-supply scenarios by blending green H_2 (with LECH of 0.37 kg CO_2-eq/kg H_2 [62], from PV-driven water electrolysis) with SMR-derived H_2 (8.43 kg CO_2-eq/kg H_2 [16]), at green H_2 fractions of 20% (S-0.2), 40% (S-0.4), 60% (S-0.6), and 80% (S-0.8). These mixes reflect evolving low-carbon hydrogen pathways and market share.

Because different mathematical expressions are involved in the mapping function (machine learning models and DPM), heuristic optimizers excel at exploring complex search spaces without requiring gradient information [63]. Specifically, well-established genetic algorithms (GA), particle swarm optimization (PSO), and simulated annealing algorithm (SA) are used to solve the optimization problems of complex waste-to-energy processes. The brief introduction of these algorithms is shown below, and Figure 4 demonstrates the core procedures.

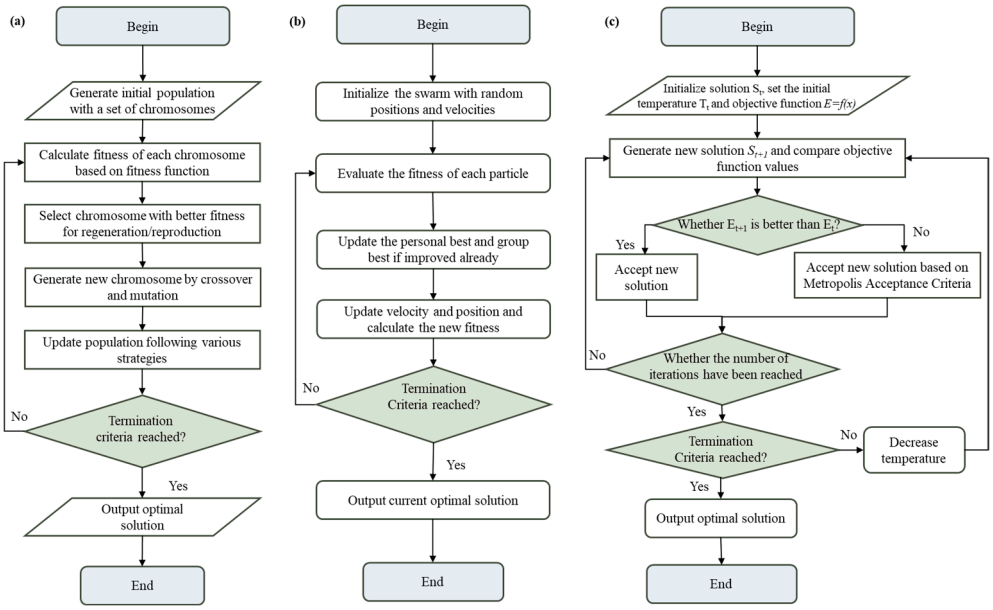

Figure 4. The general operation procedures of (**a**) GA; (**b**) PSO; and (**c**) SA.

2.5.1. Genetic Algorithms (GAs)

GAs are a series of optimization algorithms inspired by the evolution process. The behaviors of a chromosome during its generation process, such as selection, crossover, and mutation, are simulated to obtain the optimal solution with best fitness. The general operation procedures are shown in Figure 4a [64]. The population is initialized at the beginning to obtain a series of random solutions. Then, after evaluation based on fitness function, the individuals with superior fitness will be selected to generate a new population

after crossover and mutation. Roulette wheel selection is a commonly used selection method, which is conducted based on the fitness value of each individual. The selection probability of individual can be calculated using Equation (28) [65]. If the termination conditions have been satisfied, the process will end. If not, the process will go back to evaluation step and repeat the former steps.

$$P_i = \frac{f_i}{\sum_{j=1}^{n} f_j},\ j = 1, 2, \ldots, n \tag{28}$$

where the P_i is the selection probability, f_i is the fitness value of individual i, and n is the population number.

2.5.2. Particle Swarm Optimization (PSO)

PSO is inspired by the teaming behaviors in nature, such as bird flocks or fish schools, modeling the process of searching for optimal solution or near-optimal regions by sharing group information among individuals, which will allow the swarm to converge toward optimal solutions or near-optimal solutions. At the beginning of a general PSO process, the population with N particles is initialized, and each particle i has its own position (x) and velocity vector (v); then, fitness is evaluated based on the fitness function (objective function) and the current position will be updated based on the inertia, as well as the individual optimal value (p_i) and global optimal value (p_g), as shown in Equations (29) and (30) [66]. After updating individual and global optimal values, the stopping condition will be checked. If it is satisfied, the final optimal solution can be obtained, which is also the global best position.

$$v_i^{k+1} = \omega v_i^k + c_1 r_1 \left(p_i - x_i^k \right) + c_2 r_2 \left(p_g - x_i^k \right) \tag{29}$$

$$x_i^{k+1} = x_i^k + v_i^{k+1} \tag{30}$$

where x_i^k and v_i^k denote the position and the instantaneous velocity of the particle i in iteration k. ω is the inertia weight, c_1 and c_2 are the acceleration coefficient, and $r_1,\ r_2 \in [0,\ 1]$ are random scalars that introduce stochasticity.

2.5.3. Simulated Annealing Algorithm (SA)

An SA is a probabilistic global optimization algorithm inspired by the solid annealing process, which has a better performance in avoiding local optima since worse solutions can be accepted with certain probability. Based on the Metropolis acceptance criterion [67], the probability of acceptance will be higher when the temperature (T) is higher at the initial stage. As time passes, the temperature will decrease; so, the probability of acceptance for the poor solution will also decrease [68]. Equation (2), representing the time for probability of acceptance, is shown below:

$$P_{SA} = \begin{cases} 1 & E_{t+1} < E_t \\ e^{\frac{-(E_{t+1} - E_t)}{t}} & E_{t+1} > E_t \end{cases} \tag{31}$$

where the P_{SA} is the probability of acceptance, t is the current temperature, and the E is the fitness value at corresponding temperature.

To balance solution quality with computational cost, the maximum stable evolution step is used as the stopping criteria [49], or when the elapsed runtime reaches one hour, whichever comes first. The other parameters involved in these algorithms follow default settings recommended by MATLAB.

3. Results and Discussion

Within the design space, the five input variables were sampled randomly and each sample was evaluated via the detailed process simulation and LCA calculation to yield the corresponding CEF. In total, 2000 data points were generated. As depicted in Figure 5, the CEF values ranged from 0.8246 to 4.7131 kg CO_2-eq per kg MW, with a mean value of 2.6571 kg CO_2-eq/kg MW and a standard deviation of 0.7312 kg CO_2-eq/kg MW. This wide dispersion shows the strong sensitivity of process emissions to operating conditions and LCEH. Given that the average CEF remains relatively high, optimization is essential to identify operating conditions that substantially lower lifecycle emissions and improve the environmental performance of the WM-to-FT fuel process.

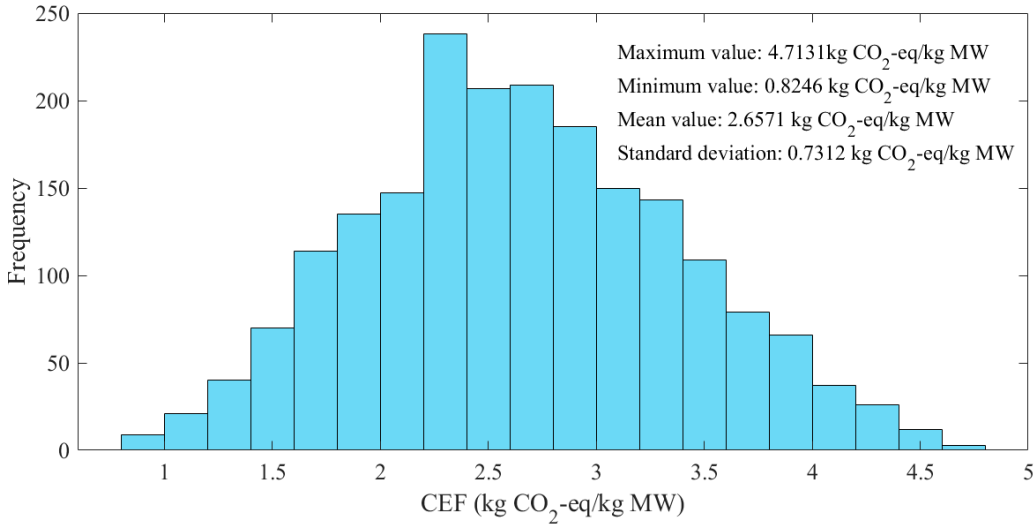

Figure 5. CEF distribution of the collected data.

Since the machine learning techniques used involve quite a few hyperparameters which make a difference in model performance, the main parameters were tuned using five-fold cross-validation during model development for improving model's robustness. At the same time, in order to more comprehensively test the effects of machine learning, each algorithm's sensitivity was further assessed according to the size of the training dataset by varying the number of samples from 200 to 2000 (in increments of 300). This range was selected to balance both data-scarce (200 samples) and well-sampled (2000 samples) regimes while maintaining computational feasibility across the studied model complexities. A step size of 300 is sufficient to reveal the impact of dataset size, and the cross-validation standard deviation (Std) is plotted as error bars. With similar accuracies, the model with a compact structure would be determined in parameter selection for reducing the computational effort. In SVM, the performances of several common kernel functions, as introduced in Section 2, were compared. The results are shown in Figure 6. It can be clearly seen that nonlinear kernels consistently outperform the linear kernel (with an R^2 over 0.87 and an RMSE below 0.25 kg CO_2-eq/kg MW). This reflects the nonlinear characteristics underlying the dataset. Considering both predictive accuracy and stability across sample sizes, a polynomial kernel of degree 2 (polynomial2) was selected for subsequent optimization. In ANN, neural networks with identical widths per hidden layer but varying depths (1–6 layers) and widths (10–30 neurons) were evaluated, as shown in Figure A1. Essentially, deeper architectures improve performance stability across datasets, while wider layers (more neurons within a layer) are beneficial for average accuracy. However, marginal gains diminished beyond increasing layers or increasing neurons per layer, with an R^2 approaching 0.9 and an RMSE approaching 0.245 kg CO_2-eq/kg MW. Consequently, a 3-layer network with 30 neurons

each (circled in red shown in Figure A1) was adopted due to its satisfactory performance in both accuracy and stability. In GPR, the performances of RBF, Matern 3/2, rational quadratic (RQ), and automatic relevance determination squared-exponential (ARDSE) kernels were compared. The ARDSE kernel yields the highest R^2 (>0.87) and lowest RMSE (<0.245 kg CO_2-eq/kg MW), as demonstrated in Figure A2, likely because its individual length scales adaptively weight each input dimension [52,69]; so, it was selected for GPR in further analysis. Using similar hyperparameter selection criteria, the tree's maximum depth (2–8) and minimum child weight (1–5) were tuned for XGBoost [70]. The results are shown in Figure A3. A maximum depth of 2 and a minimum child weight of 2 struck the best balance between bias and stability (circled in red), as indicated by cross-validated metrics (with an R^2 of ~0.85 and an RMSE of ~0.26 kg CO_2-eq/kg MW).

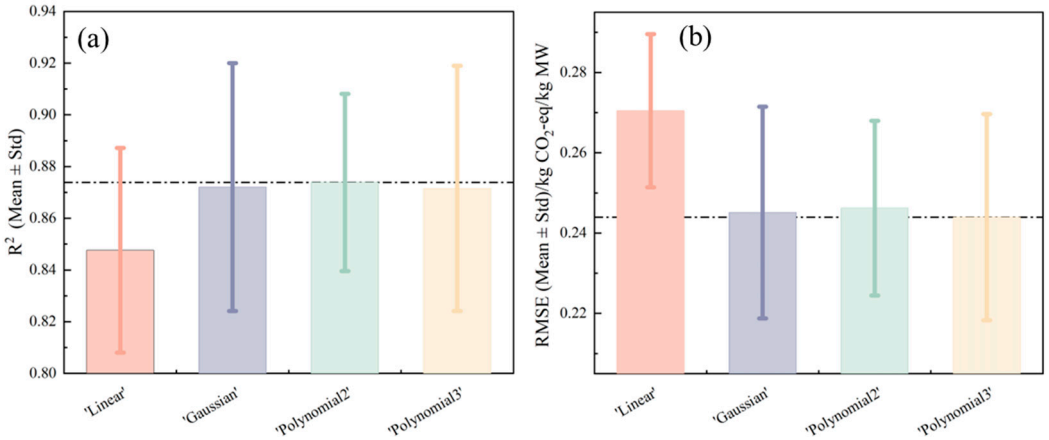

Figure 6. Cross-validation performance (R^2 and RMSE) of SVM surrogates across varying training-set sizes: (**a**) R^2, (**b**) RMSE (the colored bars and error bars represent mean values and the standard deviations as the number of training samples varies. The dotted lines in (**a**,**b**) highlight the highest R^2 and the lowest RMSE, respectively).

Based on the determined hyperparameters for each machine learning technique, each model's accuracy on both the training and test sets was evaluated (see Figure 7). All four machine learning techniques achieved high training fidelity, with an R^2 exceeding 0.9 and satisfactory generalization within the test set (with R^2 close to 0.88). XGBoost, in particular, obtained an almost perfect training performance ($R^2 \approx 1$), highlighting its ability to capture complex feature interactions. Although its test R^2 is obviously lower than that in the training set, showing evidence of modest overfitting, it remains comparable to other models', with a test R^2 of ~0.88. In comparison, SVM shows relatively lower training accuracy, reflecting limited ability to capture highly complex interactions, but benefited from strong regularization, which reduced variance. GPR stands out by combining competitive accuracy with principled predictive variance, which reduces risky extrapolation (relatively high test R^2). To contextualize these results, each surrogate model was compared against a simple linear regression baseline using RMSE, MAE, and MRE as metrics. Table 1 presents the results. Machine learning models demonstrate a certain degree of improvement over the linear fit (with an RMSE < 0.27, MAE < 0.17 and MRE < 0.0711), confirming that nonlinear, data-driven approaches better capture the complex relationships between operating conditions and the resulting carbon emission within an MW-to-FT fuel process. It is worth noting that as this is a newly designed process, there is currently no actual data on the complete process available. Therefore, this paper introduces Gaussian errors into the simulation dataset to reflect the fluctuations in actual scenarios, which may introduce bias compared to actual operating conditions.

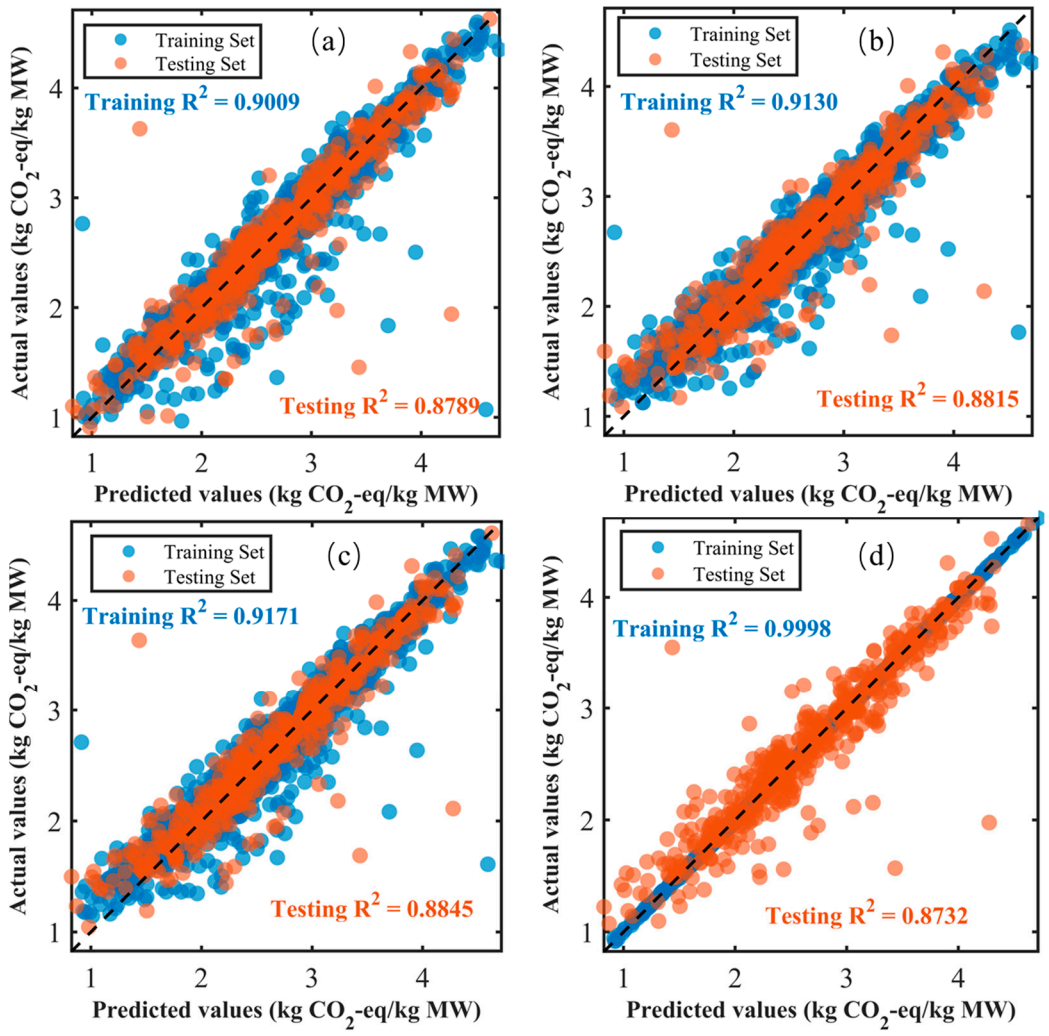

Figure 7. Performances of different machine learning models: (**a**) SVM, (**b**) ANN, (**c**) GPR, (**d**) XGBoost.

Using the obtained machine-learning-based surrogate models, operating parameters' optimization was conducted under the four hydrogen-mix scenarios considered; then, the surrogate-derived optima were validated by inputting them into the high-fidelity DPM and performing the LCA calculation to determine the final CEF. To account for the stochastic nature of heuristic optimization (GA, PSO, SA), each algorithm was run three times per model. As shown in Figure 8, the bars indicate the optimal CEF's mean of repeated optimization, while the error bars denote the standard deviation of repeated optimization. Regarding S-0.2, all methods, including machine-learning-based and DPM-based optimization, converge to a similar minimum CEF of ~1.3 kg CO_2-eq/kg MW. Under a scenario of high LCEH, this underscores the improvement in CEF after optimization. The results of S-0.4, S-0.6 and S-0.8 are presented in Figures A4–A6. Similar to S-0.2, the results of machine-learning-driven searches are close to or even slightly better than the DPM baseline, confirming that the machine learning models reliably locate the best operating conditions compared to DPM. Regarding the variability in optimization for each scenario, a machine learning + PSO scheme is highlighted, with almost the same CEF for each repeated run. In contrast, PSO on the DPM showed larger scatter, likely because the maximum running time was reached before the true convergence. For GA and SA, generally, optimization based on DPM is still less stable than that based on machine learning. By comparing all optimization algorithms, the results reveal that PSO is the most compatible with the studied machine

learning models, delivering both the lowest CEF and near-zero run-to-run variability, which has also been outlined in previous work [16]. Overall, these findings demonstrate that machine learning surrogates not only reproduce the solutions close to the DPM optimum but show better stability, highlighting their promise for reliable process optimization in waste-to-energy applications.

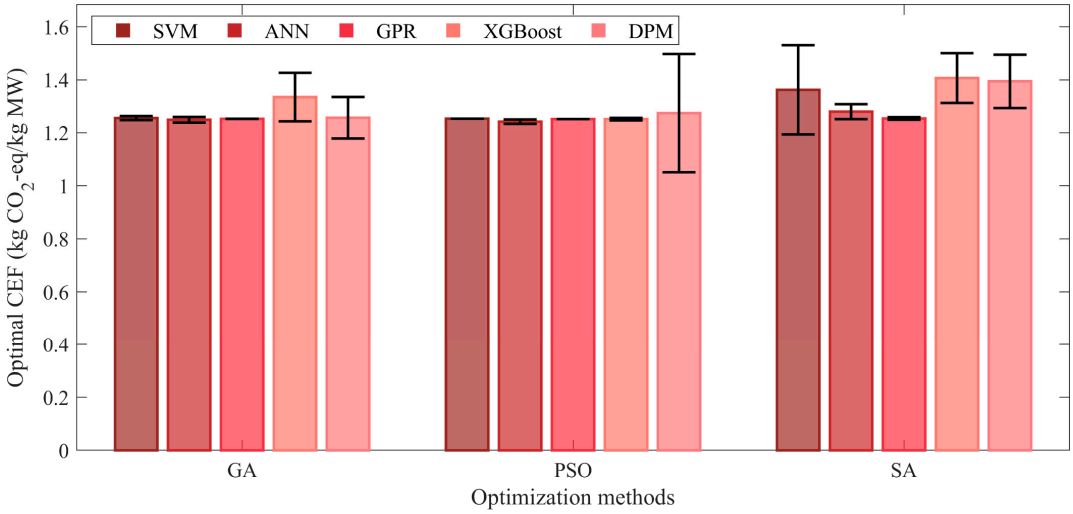

Figure 8. Optimization results of different optimization schemes under S-0.2 (the colored bars and error bars represent mean values and the standard deviations across replicate optimization runs).

In order to explore the efficiency of different optimization schemes, the running time required for optimization was analyzed in detail. Figure 9 shows the comparison results under S-0.2. The comparison results in other scenarios are shown in Figures A7–A9. Obviously, optimizations based on DPM are markedly slower than those relying on machine learning surrogates. In particular, the GA + DPM and PSO + DPM optimizations reach the maximum allowed runtime (1 h), indicating that these algorithms terminated prematurely due to time constraints rather than convergence. This highlights the substantial computational burden associated with population-based heuristics when applied to first-principle-based simulations. Notably, obvious standard deviation is observed on the combination of PSO + DPM (see Figures 9 and A7–A9), which can be attributed to the PSO algorithm's high sensitivity to the initial solution, as previously reported [71]. When the randomly generated initial solution is optimal (for example, when the initial individual is close to a minimum), optimization converges rapidly. Otherwise, convergence may not be achieved within the maximum runtime. While the SA algorithm showed a relatively better runtime performance among DPM-based methods under different scenarios, this improvement is attributed to its single-point search mechanism, as introduced in Section 2, which requires fewer evaluations per iteration. Nevertheless, even SA-based optimization still requires hundreds of seconds for optimization on average, underscoring the inefficiency of relying solely on detailed simulation models for large-scale parametric optimization, especially for complex processes.

In comparison, machine-learning-based optimizations show outstanding efficiency, with seconds to tens of seconds for optimization. This improvement arises because machine learning models reduce the computational cost of each objective evaluation, enabling the optimizer to explore a broader feasible range within the same runtime. However, differences emerge among surrogate types that affect both runtime and the reliability of optimized solutions. Notably, the combination of GPR and PSO achieves exceptional performance, basically converging within a second. This efficiency can be attributed to the synergy between GPR's compact predictive cost with uncertainty estimation and the

population-based global search capability of PSO. The optimization efficiency is highlighted by comparison with previous studies. Earlier works have shown that while rigorous models can be used to find optimal operating parameters, optimization requires thousands of simulations [32,72], resulting in optimization times on the order of hours. To improve optimization efficiency, a simplified poly-generation system of a municipal solid waste model was employed but solving it using a mixed-integer nonlinear programming solver still required optimization times of nearly 300 s [73].

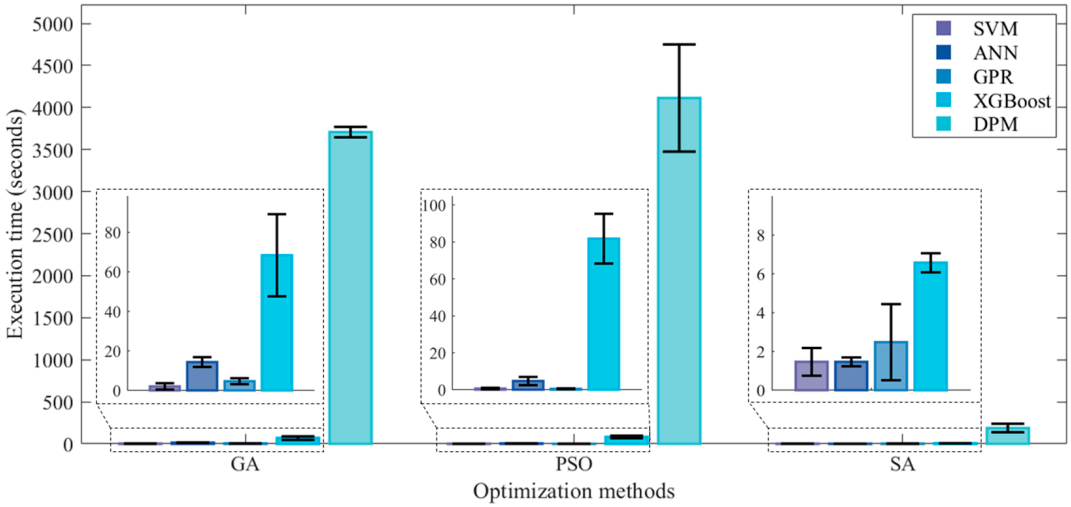

Figure 9. Execution time required for different optimization schemes under S-0.2 (the colored bars and error bars represent the mean values and standard deviations across replicate optimization runs).

Although XGBoost consistently achieves competitive optimization outcomes, its runtime is comparatively higher than those of other machine learning techniques. This performance gap is explained primarily by differences in model architecture and per-call complexity. XGBoost predictions require traversing an ensemble of decision trees (one tree per boosting round); so, per-sample latency scales with the number of trees and tree depth. To further investigate this, the average prediction times of the four machine learning models were compared (as shown in Figure 10). XGBoost required approximately 0.05 s per prediction, markedly higher than the time required by SVM, ANN, and GPR, all of which completed inference in under 0.002 s. Because population-based optimizers evaluate numerous objective functions, even modest increases in per-call latency can lead to substantial increases in total optimization time. Supported by the reliability of the rigorous process model, our findings confirm that machine learning models can act as highly accurate surrogates, showing their strong potential for predicting process performance in real-world applications. Especially of note, when multiple optimization runs are required, such as uncertainty quantification, sensitivity analysis, or multi-scenario decision-making, the ability to replace time-consuming simulations with fast, high-fidelity models can drastically accelerate workflow efficiency. As such, incorporating high-performance machine learning surrogates into early-stage process design is not only practical but essential for advancing carbon-neutral waste management and enabling robust and efficient decision-making in industrial systems.

Table 2 presents the comparison of different machine learning techniques in modeling and optimization. GPR achieves a strong balance of accuracy (R^2 of 0.917 for training and 0.885 for testing) and fast prediction latency, although exact GPR can face scalability issues when a very large dataset is involved. Notably, careful hyperparameter tuning is required for performance improvement, especially for ANN. XGBoost achieves near-perfect training accuracy (R^2 of around 0.9998) but exhibits modest overfitting and substantially

higher prediction latency due to its ensemble of decision trees. Overall, GPR shows the best trade-off between accuracy, robustness, and computational efficiency (for process optimization) in this case study.

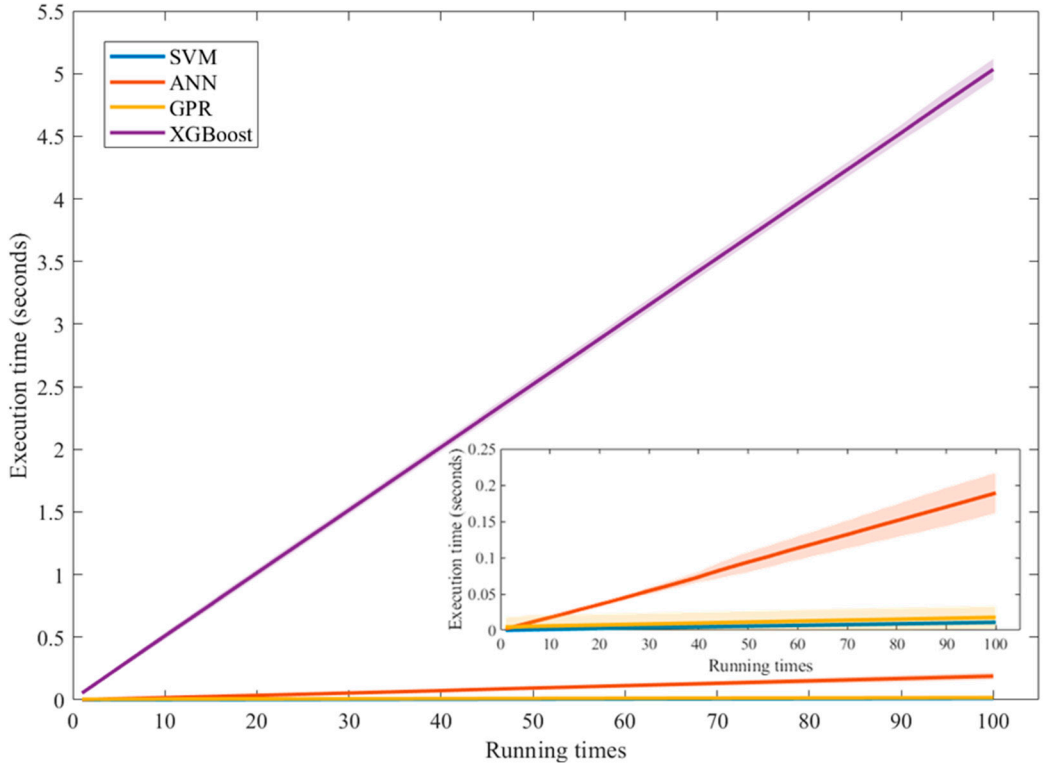

Figure 10. Execution time of running machine learning models for prediction (the shaded areas denote the standard deviation across 10 repeated runs).

Table 2. Summary of machine learning models' performances.

Models	Paradigms	Prediction Latencies (s/100 calls) *	Training Performances (R^2)	Test Accuracies (R^2)	Main Technical Limits
SVM	Kernel-based	0.0103–0.0118	0.9009	0.8789	Less expressive for very complex and high-dimensional relationships.
ANN	Connectionist	0.1617–0.2172	0.9130	0.8851	Requires careful hyper-parameter tuning, regularization, and larger datasets for stability.
GPR	Probabilistic	0.0021–0.0337	0.9171	0.8845	Scalability with large training set is limited for exact GPR.
XGBoost	Ensemble	4.9508–5.1171	0.9998	0.8732	Per-call latency higher (many trees) and modest overfitting risk without regularization.

* Based on the computational environment of this study.

Figure 11 presents the optimization results under each hydrogen-mix scenario, with error bars indicating the range of optima across different optimization schemes. In addition, the black line traces the CEF for conventional mask disposal from pure landfilling (1.1821 kg CO_2-eq/kg MW) to full incineration (1.4874 kg CO_2-eq/kg MW) [16,74]. As the fraction of green H_2 increases (the LECH decreases), the optimized CEF of the designed MW-to-FT process drops from about 1.3 to under 1.1 kg CO_2-eq/kg MW. This trend highlights the critical role of low-carbon hydrogen sourcing in emission reduction in waste valorization. The variation in CEF across all optimizations (measured by error bars) demonstrates that opti-

mal CEF is sensitive to operating conditions and thus effective optimization is essential for uncovering a process's true potential. In our four scenarios, the DPM-based optimizations with GA and PSO consumed over four hours in total (shown in see Figures 9 and A7–A9), compared to under one minute when using machine learning surrogates. Given more optimizations are demanded in robust process design, this highlights the importance of efficiency in optimization. Regarding the results, as 40% green hydrogen is provided, the designed MW-to-FT fuel process becomes the most favorable conventional pathway (pure landfilling), offering carbon reduction and the avoidance of other landfill-related pollution risks [75]. Beyond environmental benefits, this waste-to-energy conversion follows the circular economy and provides new revenue from fuel production and selling [32]. Overall, these results confirm that a well-tuned machine-learning-assisted optimization framework can deliver superior, low-carbon solutions for MW treatment.

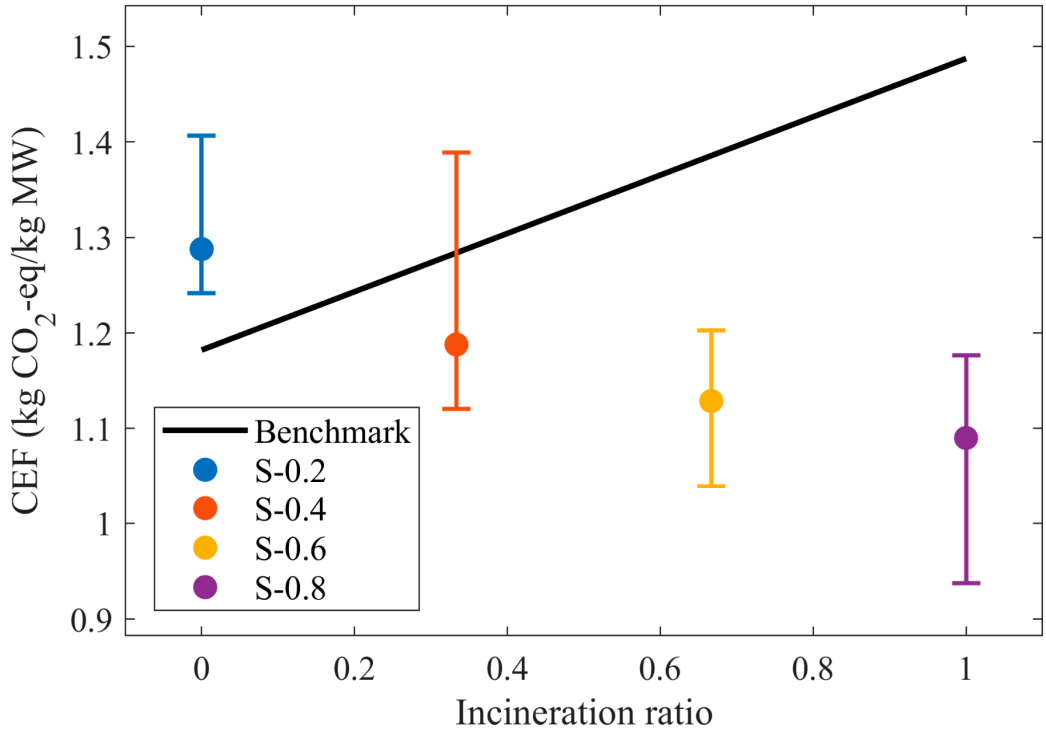

Figure 11. Comparison of CEF between the proposed MW-to-FT process and conventional treatment routes. (Error bars indicate the maximum and minimum optimal CEFs determined by different optimization methods under each scenario and the black line indicates how CEF varies with the landfill-to-incineration split).

4. Conclusions, Limitations and Outlook

This study develops a comprehensive process for converting MW into FT fuel and quantifies the CEF using cradle-to-gate LCA. Integrating rigorous process simulation with LCA, a dataset covering diverse operating conditions, LCEH and CEF, is constructed for machine learning. Four distinct machine learning surrogate models (SVM, ANN, GPR, XGBoost) are constructed after tuning hyperparameters via cross-validation, each achieving high accuracy with test R^2 of around 0.9. Coupling these models with heuristic algorithms (GA, PSO and SA), operation optimizations are performed under varying green-H_2-blending scenarios (20–80%) and show identical or even lower CEF (~1.3 to ~1.1 kg CO_2-eq/kg MW) compared to optimization based on DPM, but at a dramatically lower computational cost (<1–30 s versus hundreds to thousands of seconds). In particular, the combination of GPR and PSO demonstrates the best performance with satisfactory accuracy, efficiency and stability. Further analysis identifies the time for model execution as the main

driver of optimization efficiency. Sensitivity analysis shows that as LECH decreases, the optimized CEF consistently falls below the landfill and incineration benchmarks, confirming the designed MW-to-FT fuel process's environmental advantage. Our results demonstrate that machine learning surrogates can match mechanism-based model in accuracy while delivering gains within orders of magnitude in optimization speed and robustness, which is critical for accelerating process design and potential assessment under uncertainty.

Despite these promising results, several limitations remain. The success of ML surrogates relies on the availability of a rigorous and high-fidelity process model. For broader applicability, future studies should integrate experimental datasets to ensure that trained models are capable of capturing real-world process variability. In addition, variability in MW composition poses challenges for scale-up, necessitating adaptive retraining of ML models to maintain reliability under dynamic conditions. More efficient sampling strategies (e.g., Latin hypercube or stratified sampling) could further improve training data quality, while introducing controlled noise may help capture operational uncertainties in the real world. Addressing these aspects will be critical to advancing the proposed framework into practice, supporting reliable and scalable low-carbon MW-to-energy deployment.

Author Contributions: Conceptualization, J.Z. and J.R.; Methodology, J.Z., J.L. and J.R.; Software, C.H.; Validation, J.Z., J.L., J.R. and C.H.; Formal Analysis, J.Z. and J.R.; Investigation, J.Z.; Resources, J.R.; Data Curation, J.Z.; Writing—Original Draft, J.Z.; Writing—Review and Editing, J.L., J.R. and C.H.; Supervision, J.R.; Project Administration, J.R.; Funding Acquisition, J.R. All authors have read and agreed to the published version of the manuscript.

Funding: The work described in this study received support from a grant from the Research Committee of The Hong Kong Polytechnic University under the student account code RKQ1. The work described in this paper was mainly supported by funding support from the Research Institute for Advanced Manufacturing (RIAM) of The Hong Kong Polytechnic University (1-CDLY, Project ID: P0056082), and the work was supported by a grant from the Departmental General Research Fund (Grant No. 4-ZZXD, Project ID: P0056352). The authors would like to express their sincere thanks for the financial support from the Research Institute for Advanced Manufacturing (RIAM) of The Hong Kong Polytechnic University (project code: 1-CDK2, Project ID: P0050827). The work described in this paper was also supported by a grant from Research Grants Council of the Hong Kong Special Administrative Region, China-General Research Fund (Project ID: P0042030, Funding Body Ref. No: 15304222, Project No. B-Q97U), a grant from the Research Institute for Advanced Manufacturing (RIAM), The Hong Kong Polytechnic University (PolyU) (Project No. 1-CD4J, Project ID: P0041367), and a grant from the Environment and Conservation Fund (ECF) (Project ID: P0043333, Funding Body Ref. No: ECF 51/2022, Project No. K-ZB5Z).

Data Availability Statement: The raw data supporting the conclusions of this article will be made available by the authors on request.

Acknowledgments: During the preparation of this manuscript, DeepSeek was used for the purposes of grammar checking.

Conflicts of Interest: The authors declare no conflicts of interest.

Appendix A

Table A1. Proximate and ultimate analysis of MW [76].

Items	Compositions	Values
Proximate analysis (wt.%) [a]	Moisture	5.00
	Ash	0.20
	Volatiles	92.90
	Fixed carbon	1.90
Ultimate analysis (wt.%) [b]	C	84.17
	H	14.93
	O	0.7
Higher heating value (MJ/kg) [c]	-	46.9

[a]: as-received basis; [b]: dry basis; [c]: raw basis.

Table A2. Key operating parameters involved in process simulation [16,18,32,33,37].

Processes	Operating Conditions	Values	Units
Plasma gasification	Temperature	2000–3000	°C
	Equivalent ratio (ER)	0.1–0.5	-
	Steam-to-waste ratio (SWR)	0.5–1	-
RWGS	Temperature	600	°C
	Pressure	24.5	bar
	CO_2 conversion rate	36	%
FT synthesis	Temperature	220	°C
	Pressure	30	Bar
	Splitting ratio of light gases (LGSR)	0–1	-
PSA	H_2 purity	99.9	%
	H_2 recovery rate	85	%
	Duty	0.657	kWh/kg
Combined heat and power generation	Combustion temperature	900	°C
	Inlet pressure of turbine	70	Bar
	Outlet pressure of turbine	7	kPa
MEA-based carbon capture	Capture efficiency	85	%
	Duty	4	MJ/kg

Table A3. Process simulation results of a base case.

Items	MW	H_2O	O_2	S1	S2	S3	S4	Water-1	S5	S6	S7	S8	S9	S10	S11	S12
Temperature	25.00	25.00	25.00	2500.00	25.00	18.80	2500.00	25.00	25.00	43.30	150.00	600.00	600.00	140.00	140.00	140.00
Pressure	1.00	1.00	1.00	1.00	1.00	1.00	1.00	1.00	1.00	1.00	24.20	24.20	24.20	24.20	24.20	24.20
Mass flowrate	1000.00	750.00	1030.00	2780.00	2780.00	1780.00	1780.00	615.00	2160.00	4220.00	4220.00	4220.00	4220.00	4220.00	1210.00	3010.00
X_{MW}	1.00	0.00	0.00	0.00	0.00	0.00	0.00	0.00	0.00	0.00	0.00	0.00	0.00	0.00	0.00	0.00
X_{H2}	0.00	0.00	0.00	0.42	0.42	0.00	0.00	0.00	0.52	0.45	0.45	0.45	0.36	0.36	0.00	0.42
X_{O2}	0.00	0.00	1.00	0.00	0.00	0.44	0.44	0.00	0.00	0.00	0.00	0.00	0.00	0.00	0.00	0.00
X_{CH4}	0.00	0.00	0.00	0.00	0.00	0.00	0.00	0.00	0.00	0.00	0.00	0.00	0.00	0.00	0.00	0.00
X_{CO}	0.00	0.00	0.00	0.34	0.34	0.00	0.00	0.00	0.42	0.29	0.29	0.29	0.38	0.38	0.00	0.44
X_{CO2}	0.00	0.00	0.00	0.03	0.03	0.00	0.00	0.00	0.03	0.24	0.24	0.24	0.15	0.15	1.00	0.03
X_{H2O}	1.00	1.00	0.00	0.21	0.21	0.56	0.56	1.00	0.03	0.02	0.02	0.02	0.11	0.11	0.00	0.12
Items	**S13**		**S14**	**S15**	**S16**	**S17**	**S18**	**S19**	**S20**	**S21**	**S22**	**S23**	**S24**	**Wax**	**Naphtha**	**Jet fuel**
Temperature	187.00		150.00	220.00	25.00	25.00	220.00	25.00	25.00	25.00	25.00	5.74	5.74	5.74	5.74	5.74
Pressure	0.58		29.60	29.60	0.53	0.53	29.60	0.58	0.58	0.58	0.58	0.53	0.53	0.53	0.53	0.53
Mass flowrate	4010.00		4010.00	4010.00	2370.00	1640.00	2370.00	1610.00	754.00	807.00	807.00	3200.00	2900.00	301.00	219.00	224.00
X_{H2}	0.60		0.60	0.40	0.57	0.00	0.37	0.49	0.00	0.49	0.49	0.15	0.15	0.00	0.00	0.00
X_{O2}	0.00		0.00	0.00	0.00	0.00	0.00	0.00	0.00	0.00	0.00	0.00	0.00	0.00	0.00	0.00
X_{CH4}	0.00		0.00	0.00	0.00	0.00	0.00	0.00	0.00	0.00	0.00	0.00	0.00	0.00	0.00	0.00
X_{CO}	0.29		0.29	0.19	0.28	0.00	0.18	0.25	0.00	0.25	0.25	0.08	0.08	0.00	0.00	0.00
X_{CO2}	0.03		0.03	0.04	0.06	0.00	0.09	0.12	0.00	0.12	0.12	0.04	0.04	0.00	0.00	0.00
X_{H2O}	0.08		0.08	0.32	0.05	0.97	0.27	0.05	0.95	0.05	0.05	0.68	0.68	0.00	0.00	0.00
X_{C1}	0.00		0.00	0.01	0.01	0.00	0.01	0.02	0.00	0.02	0.02	0.01	0.01	0.00	0.00	0.00
X_{C2}	0.00		0.00	0.01	0.01	0.00	0.01	0.02	0.00	0.02	0.02	0.01	0.01	0.00	0.00	0.00
X_{C3}	0.00		0.00	0.00	0.01	0.00	0.01	0.02	0.00	0.02	0.02	0.00	0.00	0.00	0.00	0.00
X_{C4}	0.00		0.00	0.00	0.01	0.00	0.01	0.01	0.00	0.01	0.01	0.00	0.00	0.00	0.00	0.00
X_{C5}	0.00		0.00	0.00	0.01	0.00	0.01	0.01	0.00	0.01	0.01	0.00	0.00	0.00	0.24	0.00
X_{C6}	0.00		0.00	0.00	0.00	0.00	0.01	0.01	0.00	0.01	0.01	0.00	0.00	0.00	0.22	0.00
X_{C7}	0.00		0.00	0.00	0.00	0.00	0.01	0.01	0.00	0.01	0.01	0.00	0.00	0.00	0.20	0.00
X_{C8}	0.00		0.00	0.00	0.00	0.00	0.00	0.00	0.01	0.00	0.00	0.00	0.00	0.00	0.18	0.00
X_{C9}	0.00		0.00	0.00	0.00	0.00	0.00	0.00	0.01	0.00	0.00	0.00	0.00	0.00	0.16	0.00
X_{C10}	0.00		0.00	0.00	0.00	0.00	0.00	0.00	0.00	0.00	0.00	0.00	0.00	0.00	0.00	0.24
X_{C11}	0.00		0.00	0.00	0.00	0.00	0.00	0.00	0.00	0.00	0.00	0.00	0.00	0.00	0.00	0.22
X_{C12}	0.00		0.00	0.00	0.00	0.00	0.00	0.00	0.00	0.00	0.00	0.00	0.00	0.00	0.00	0.20
X_{C13}	0.00		0.00	0.00	0.00	0.00	0.00	0.00	0.00	0.00	0.00	0.00	0.00	0.00	0.00	0.18
X_{C14}	0.00		0.00	0.00	0.00	0.00	0.00	0.00	0.00	0.00	0.00	0.00	0.00	0.00	0.00	0.16
X_{C15}	0.00		0.00	0.00	0.00	0.00	0.00	0.00	0.00	0.00	0.00	0.00	0.00	0.00	0.00	0.00
X_{C16}	0.00		0.00	0.00	0.00	0.00	0.00	0.00	0.00	0.00	0.00	0.00	0.00	0.00	0.00	0.00
X_{C17}	0.00		0.00	0.00	0.00	0.00	0.00	0.00	0.00	0.00	0.00	0.00	0.00	0.00	0.00	0.00

Table A3. *Cont.*

Items	S13	S14	S15	S16	S17	S18	S19	S20	S21	S22	S23	S24	Wax	Naphtha	Jet fuel
X_{C18}	0.00	0.00	0.00	0.00	0.00	0.00	0.00	0.00	0.00	0.00	0.00	0.00	0.00	0.00	0.00
X_{C19}	0.00	0.00	0.00	0.00	0.00	0.00	0.00	0.00	0.00	0.00	0.00	0.00	0.14	0.00	0.00
X_{C20}	0.00	0.00	0.00	0.00	0.00	0.00	0.00	0.00	0.00	0.00	0.00	0.00	0.13	0.00	0.00
X_{C21}	0.00	0.00	0.00	0.00	0.00	0.00	0.00	0.00	0.00	0.00	0.00	0.00	0.11	0.00	0.00
X_{C22}	0.00	0.00	0.00	0.00	0.00	0.00	0.00	0.00	0.00	0.00	0.00	0.00	0.10	0.00	0.00
X_{C23}	0.00	0.00	0.00	0.00	0.00	0.00	0.00	0.00	0.00	0.00	0.00	0.00	0.09	0.00	0.00
X_{C24}	0.00	0.00	0.00	0.00	0.00	0.00	0.00	0.00	0.00	0.00	0.00	0.00	0.08	0.00	0.00
X_{C25}	0.00	0.00	0.00	0.00	0.00	0.00	0.00	0.00	0.00	0.00	0.00	0.00	0.07	0.00	0.00
X_{C26}	0.00	0.00	0.00	0.00	0.00	0.00	0.00	0.00	0.00	0.00	0.00	0.00	0.07	0.00	0.00
X_{C27}	0.00	0.00	0.00	0.00	0.00	0.00	0.00	0.00	0.00	0.00	0.00	0.00	0.06	0.00	0.00
X_{C28}	0.00	0.00	0.00	0.00	0.00	0.00	0.00	0.00	0.00	0.00	0.00	0.00	0.05	0.00	0.00
X_{C29}	0.00	0.00	0.00	0.00	0.00	0.00	0.00	0.00	0.00	0.00	0.00	0.00	0.05	0.00	0.00
X_{C30}	0.00	0.00	0.00	0.00	0.00	0.00	0.00	0.00	0.00	0.00	0.00	0.00	0.04	0.00	0.00

Items	Diesel	S26	S27	Air	S28	S29	S30	S31	S32	S33	S34	S35	S36	Emitted gases	Water-2
Temperature	5.74	5.74	25.00	25.00	25.00	900.00	40.00	859.00	104.00	30.00	30.60	40.00	40.00	25.00	25.00
Pressure	0.53	0.53	1.00	1.00	1.00	1.00	1.00	69.10	0.07	0.04	69.10	1.00	1.00	1.00	1.00
Mass flowrate	154.00	2300.00	627.00	2540.00	35.70	3170.00	3170.00	859.00	859.00	859.00	859.00	2350.00	815.00	2130.00	223.00
X_{MW}	0.00	0.00	0.00	0.00	0.00	0.00	0.00	0.00	0.00	0.00	0.00	0.00	0.00	0.00	0.00
X_{H2}	0.00	0.16	0.14	0.00	1.00	0.00	0.00	0.00	0.00	0.00	0.00	0.00	0.00	0.00	0.00
X_{O2}	0.00	0.00	0.00	0.21	0.00	0.01	0.01	0.00	0.00	0.00	0.00	0.01	0.00	0.01	0.00
X_{CH4}	0.00	0.00	0.00	0.00	0.00	0.00	0.00	0.00	0.00	0.00	0.00	0.00	0.00	0.00	0.00
X_{C2H4}	0.00	0.00	0.00	0.00	0.00	0.00	0.00	0.00	0.00	0.00	0.00	0.00	0.00	0.00	0.00
X_{C2H6}	0.00	0.00	0.00	0.00	0.00	0.00	0.00	0.00	0.00	0.00	0.00	0.00	0.00	0.00	0.00
X_{CO}	0.00	0.08	0.47	0.00	0.00	0.00	0.00	0.00	0.00	0.00	0.00	0.00	0.00	0.00	0.00
X_{CO2}	0.00	0.04	0.22	0.00	0.00	0.21	0.21	0.00	0.00	0.00	0.00	0.04	1.00	0.04	0.00
X_{H2O}	0.00	0.70	0.05	0.01	0.00	0.14	0.14	1.00	1.00	1.00	1.00	0.17	0.00	0.03	1.00
X_{N2}	0.00	0.00	0.00	0.78	0.00	0.65	0.65	0.00	0.00	0.00	0.00	0.79	0.00	0.92	0.00
X_{C1}	0.00	0.01	0.03	0.00	0.00	0.00	0.00	0.00	0.00	0.00	0.00	0.00	0.00	0.00	0.00
X_{C2}	0.00	0.01	0.03	0.00	0.00	0.00	0.00	0.00	0.00	0.00	0.00	0.00	0.00	0.00	0.00
X_{C3}	0.00	0.01	0.03	0.00	0.00	0.00	0.00	0.00	0.00	0.00	0.00	0.00	0.00	0.00	0.00
X_{C4}	0.00	0.00	0.03	0.00	0.00	0.00	0.00	0.00	0.00	0.00	0.00	0.00	0.00	0.00	0.00
X_{C15}	0.29	0.00	0.00	0.00	0.00	0.00	0.00	0.00	0.00	0.00	0.00	0.00	0.00	0.00	0.00
X_{C16}	0.26	0.00	0.00	0.00	0.00	0.00	0.00	0.00	0.00	0.00	0.00	0.00	0.00	0.00	0.00
X_{C17}	0.24	0.00	0.00	0.00	0.00	0.00	0.00	0.00	0.00	0.00	0.00	0.00	0.00	0.00	0.00
X_{C18}	0.21	0.00	0.00	0.00	0.00	0.00	0.00	0.00	0.00	0.00	0.00	0.00	0.00	0.00	0.00

X: mole fraction.

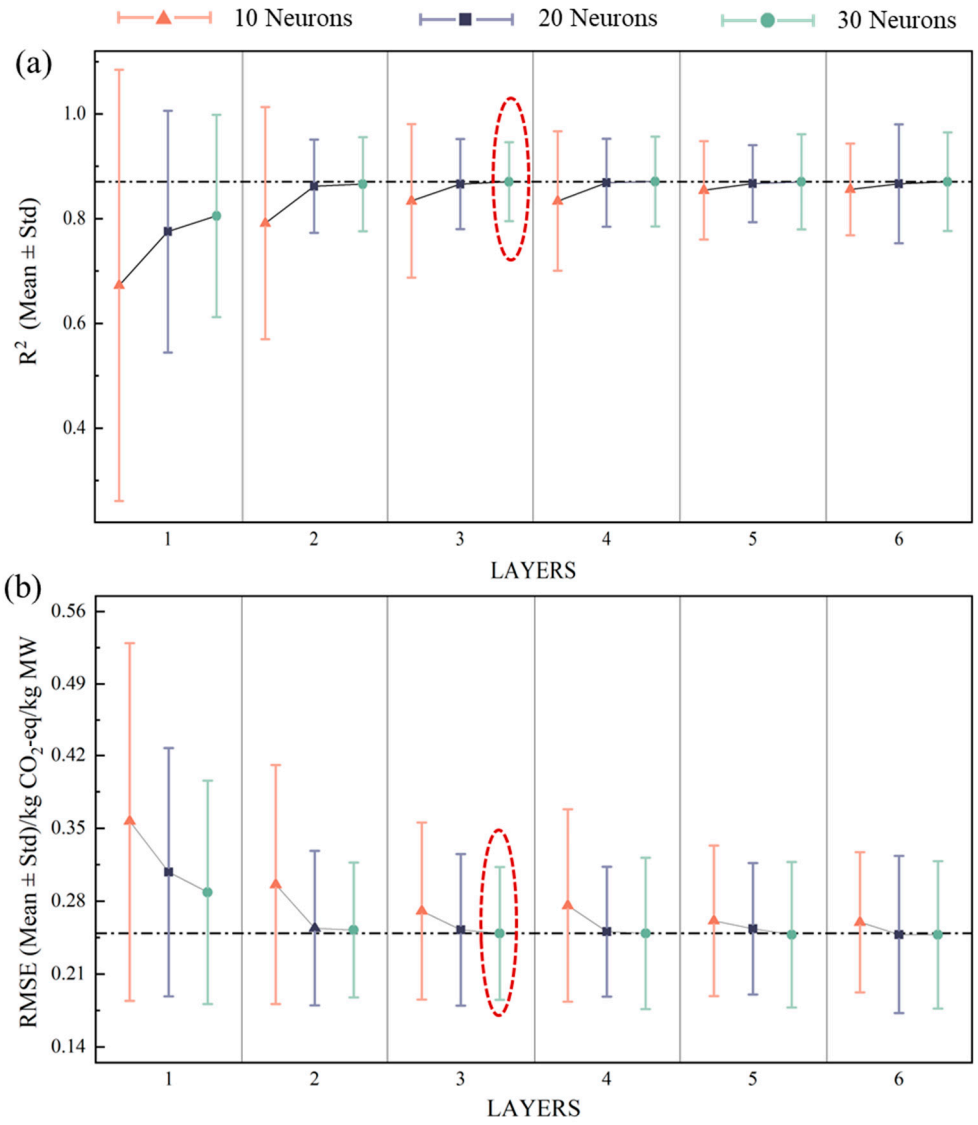

Figure A1. Cross validation results of ANN: (**a**) R^2, (**b**) RMSE. (The colored bars and error bars represent mean values and the standard deviations as the number of training samples varies. The error bars do not imply the model can actually achieve the extreme values indicated. The dotted circles highlight the optimal results).

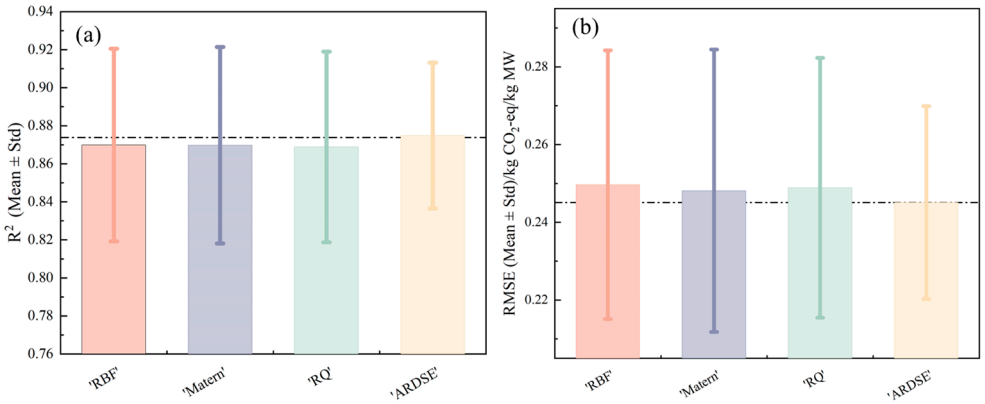

Figure A2. Cross-validation performance of GPR surrogates across varying training-set sizes: (**a**) R^2 (**b**) RMSE. (The colored bars and error bars represent mean values and the standard deviations as the number of training samples varies. The dotted lines in (**a**,**b**) highlight the highest R^2 and the lowest RMSE, respectively).

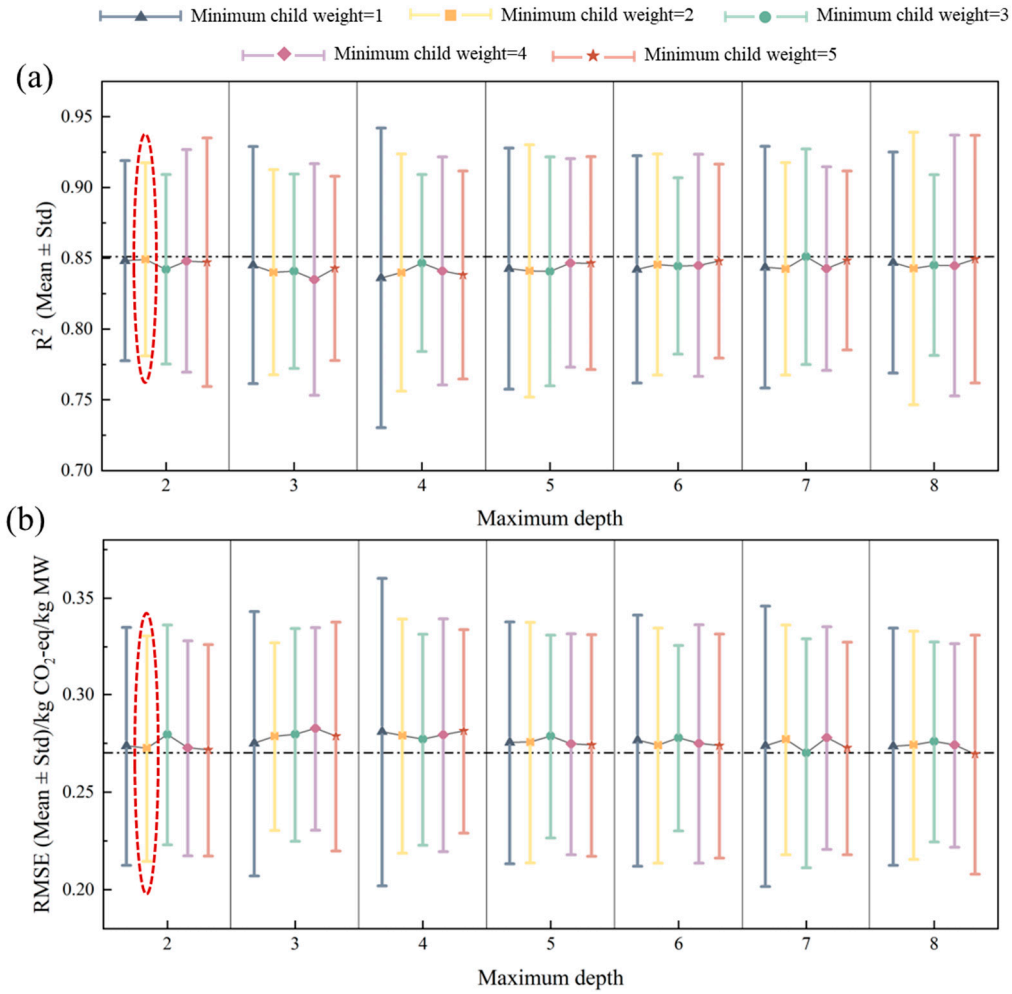

Figure A3. Cross-validation performance of XGBoost surrogates across varying training-set sizes: (**a**) R^2; (**b**) RMSE. (The colored points and error bars represent mean values and the standard deviations as the number of training samples varies. Other hyperparameters, such as learning rate, column subsample rate, and gamma value, follow the previous literature [70]. The dotted circles highlight the optimal results).

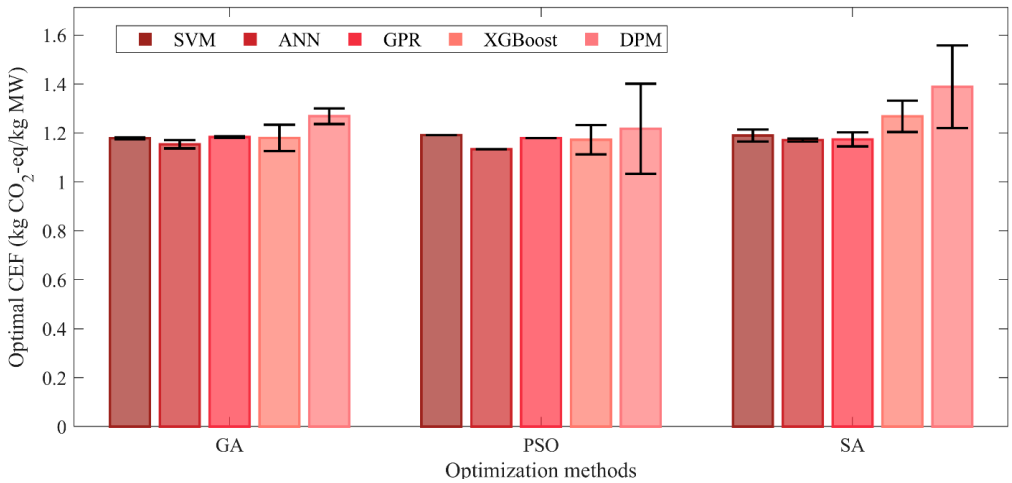

Figure A4. Optimization results of different optimization schemes under S-0.4. (The colored bars and error bars represent mean values and the standard deviations across replicate optimization runs).

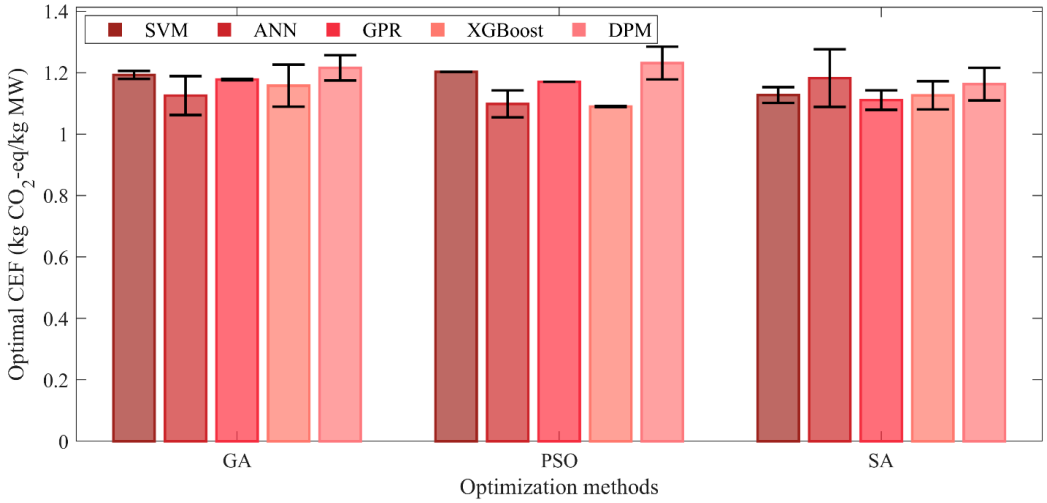

Figure A5. Optimization results of different optimization schemes under S-0.6. (The colored bars and error bars represent mean values and the standard deviations across replicate optimization runs).

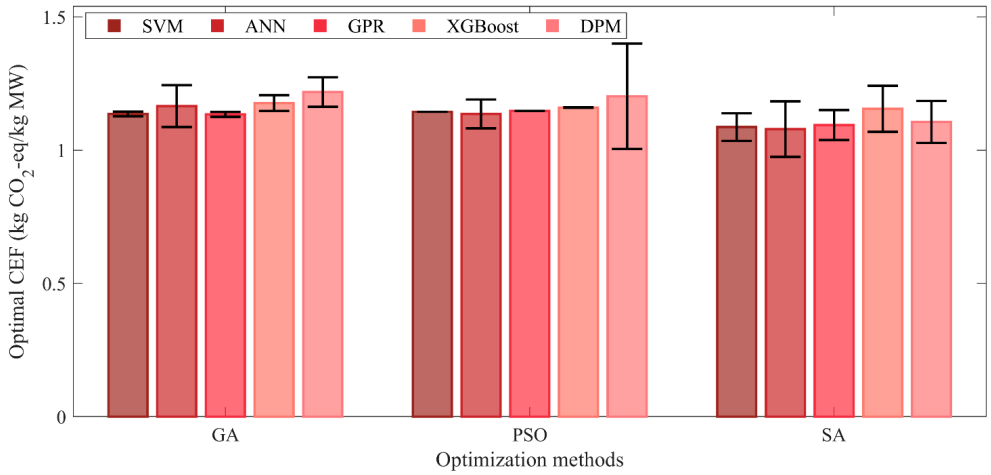

Figure A6. Optimization results of different optimization schemes under S-0.8. (The colored bars and error bars represent mean values and the standard deviations across replicate optimization runs).

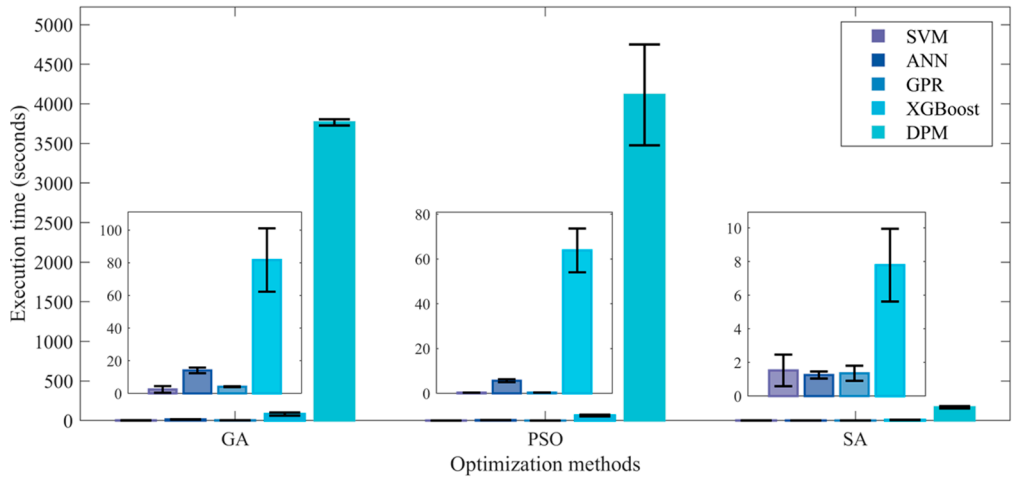

Figure A7. Execution time required for different optimization schemes under S-0.4. (The colored bars and error bars represent the mean values and standard deviations across replicate optimization runs).

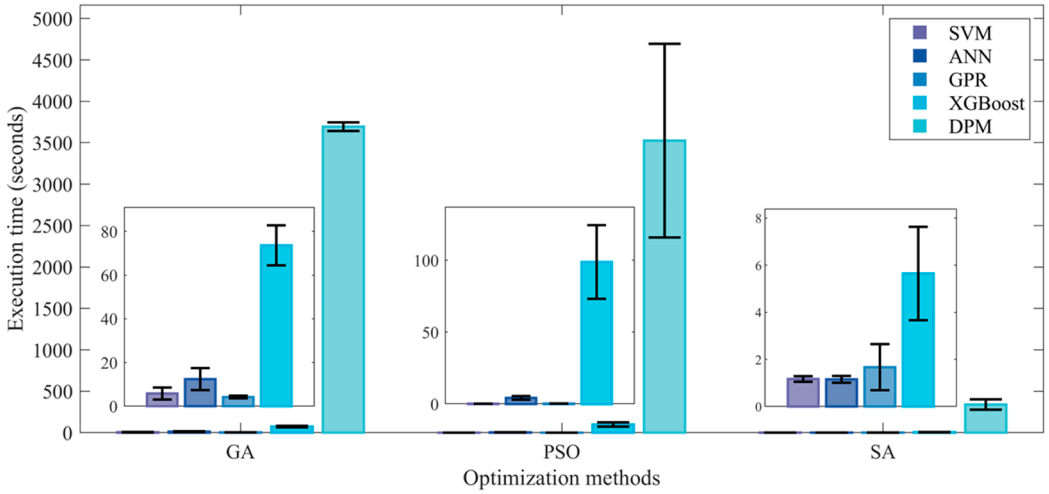

Figure A8. Execution time required for different optimization schemes under S-0.6. (The colored bars and error bars represent the mean values and standard deviations across replicate optimization runs).

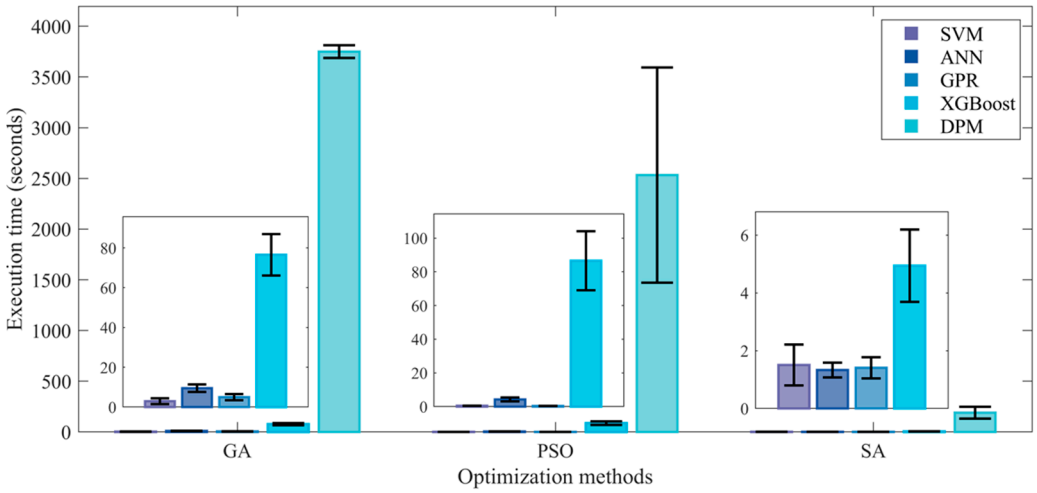

Figure A9. Execution time required for different optimization schemes under S-0.8. (The colored bars and error bars represent the mean values and standard deviations across replicate optimization runs).

References

1. Mohee, R. Medical Wastes Characterisation in Healthcare Institutions in Mauritius. *Waste Manag.* **2005**, *25*, 575–581. [CrossRef] [PubMed]
2. Liang, Y.; Song, Q.; Wu, N.; Li, J.; Zhong, Y.; Zeng, W. Repercussions of COVID-19 Pandemic on Solid Waste Generation and Management Strategies. *Front. Environ. Sci. Eng.* **2021**, *15*, 115. [CrossRef]
3. You, S.; Sonne, C.; Ok, Y.S. COVID-19's Unsustainable Waste Management. *Science* **2020**, *368*, 1438. [CrossRef]
4. Ghasemi, M.K.; Yusuff, R.B.M. Advantages and Disadvantages of Healthcare Waste Treatment and Disposal Alternatives: Malaysian Scenario. *Pol. J. Environ. Stud.* **2016**, *25*, 17–25. [CrossRef]
5. Mazzei, H.G.; Specchia, S. Latest Insights on Technologies for the Treatment of Solid Medical Waste: A review. *J. Environ. Chem. Eng.* **2023**, *11*, 109309. [CrossRef]
6. Reyes-López, J.A.; Ramírez-Hernández, J.; Lázaro-Mancilla, O.; Carreón-Diazconti, C.; Garrido, M.M.L. Assessment of Groundwater Contamination by Landfill Leachate: A Case in México. *Waste Manag.* **2008**, *28*, S33–S39. [CrossRef]
7. Mukherjee, S.; Mukhopadhyay, S.; Hashim, M.A.; Gupta, B. Sen Contemporary Environmental Issues of Landfill Leachate: Assessment and Remedies. *Crit. Rev. Environ. Sci. Technol.* **2015**, *45*, 472–590. [CrossRef]
8. Khan, M.S.; Mubeen, I.; Caimeng, Y.; Zhu, G.; Khalid, A.; Yan, M. Waste to Energy Incineration Technology: Recent Development under Climate Change Scenarios. *Waste Manag. Res.* **2022**, *40*, 1708–1729. [CrossRef]
9. Imran, M.; Jijian, Z.; Sharif, A.; Magazzino, C. Evolving Waste Management: The Impact of Environmental Technology, Taxes, and Carbon Emissions on Incineration in EU Countries. *J. Environ. Manag.* **2024**, *364*, 121440. [CrossRef] [PubMed]

10. Li, C.H.; Lee, T.T.; Lau, S.S.Y. Enhancement of Municipal Solid Waste Management in Hong Kong through Innovative Solutions: A Review. *Sustainability* **2023**, *15*, 3310. [CrossRef]
11. Zhu, J.; Fei, X.; Yin, K. Assessment of Waste-to-Energy Conversion Technologies for Biomass Waste under Different Shared Socioeconomic Pathways. *Energy Environ. Sustain.* **2025**, *1*, 100021. [CrossRef]
12. Chaiyat, N. Energy, Exergy, Economic, and Environmental Analysis of an Organic Rankine Cycle Integrating with Infectious Medical Waste Incinerator. *Therm. Sci. Eng. Prog.* **2021**, *22*, 100810. [CrossRef]
13. Su, L.; Wu, S.; Fu, G.; Zhu, W.; Zhang, X.; Liang, B. Creep Characterisation and Microstructural Analysis of Municipal Solid Waste Incineration Fly Ash Geopolymer Backfill. *Sci. Rep.* **2024**, *14*, 29828. [CrossRef]
14. Zhao, X.; You, F. Waste Respirator Processing System for Public Health Protection and Climate Change Mitigation under COVID-19 Pandemic: Novel Process Design and Energy, Environmental, and Techno-Economic Perspectives. *Appl. Energy* **2021**, *283*, 116129. [CrossRef] [PubMed]
15. Kuo, P.C.; Illathukandy, B.; Wu, W.; Chang, J.S. Plasma Gasification Performances of Various Raw and Torrefied Biomass Materials Using Different Gasifying Agents. *Bioresour. Technol.* **2020**, *314*, 123740. [CrossRef]
16. Zhou, J.; Liu, C.; Ren, J.; He, C. Targeting Carbon-Neutral Waste Reduction: Novel Process Design, Modelling and Optimization for Converting Medical Waste into Hydrogen. *Energy* **2024**, *310*, 133272. [CrossRef]
17. Li, J.; Wang, H.; Chen, H.; Wu, H.; Xu, G.; Dong, Y.; Zhao, Q.; Liu, T. Comparative Thermodynamic and Techno-Economic Analysis of Various Medical Waste-to-Hydrogen/Methanol Pathways Based on Plasma Gasification. *Appl. Therm. Eng.* **2023**, *221*, 119762. [CrossRef]
18. Zhou, J.; Ren, J.; Zhu, L.; He, C. Turning Waste into Energy through a Solar-Powered Multi-Generation System with Novel Machine Learning-Based Life Cycle Optimization. *Chem. Eng. Sci.* **2025**, *307*, 121348. [CrossRef]
19. Mehdi, M.; Ammar Taqvi, S.A.; Shaikh, A.A.; Khan, S.; Naqvi, S.R.; Shahbaz, M.; Juchelková, D. Aspen plus Simulation Model of Municipal Solid Waste Gasification of Metropolitan City for Syngas Production. *Fuel* **2023**, *344*, 128128. [CrossRef]
20. Ali, A.M.; Shahbaz, M.; Inayat, M.; Shahzad, K.; Al-Zahrani, A.A.; Mahpudz, A.B. Conversion of Municipals Waste into Syngas and Methanol via Steam Gasification Using CaO as Sorbent: An Aspen Plus Modelling. *Fuel* **2023**, *349*, 128640. [CrossRef]
21. Zhu, X.; Li, Y.; Wang, X. Machine Learning Prediction of Biochar Yield and Carbon Contents in Biochar Based on Biomass Characteristics and Pyrolysis Conditions. *Bioresour. Technol.* **2019**, *288*, 121527. [CrossRef]
22. Tang, Q.; Chen, Y.; Yang, H.; Liu, M.; Xiao, H.; Wang, S.; Chen, H.; Raza Naqvi, S. Machine Learning Prediction of Pyrolytic Gas Yield and Compositions with Feature Reduction Methods: Effects of Pyrolysis Conditions and Biomass Characteristics. *Bioresour. Technol.* **2021**, *339*, 125581. [CrossRef] [PubMed]
23. Timilsina, M.S.; Chaudhary, Y.; Shah, A.K.; Lohani, S.P.; Bhandari, R.; Uprety, B. Syngas Composition Analysis for Waste to Methanol Production: Techno-Economic Assessment Using Machine Learning and Aspen Plus. *Renew. Energy* **2024**, *228*, 120574. [CrossRef]
24. Wang, Z.; Li, J.; Rangaiah, G.P.; Wu, Z. Machine Learning Aided Multi-Objective Optimization and Multi-Criteria Decision Making: Framework and Two Applications in Chemical Engineering. *Comput. Chem. Eng.* **2022**, *165*, 107945. [CrossRef]
25. Fath, V.; Kockmann, N.; Otto, J.; Röder, T. Self-Optimising Processes and Real-Time-Optimisation of Organic Syntheses in a Microreactor System Using Nelder–Mead and Design of Experiments. *React. Chem. Eng.* **2020**, *5*, 1281–1299. [CrossRef]
26. Diehl, M.; Bock, H.G.; Schlöder, J.P.; Findeisen, R.; Nagy, Z.; Allgöwer, F. Real-Time Optimization and Nonlinear Model Predictive Control of Processes Governed by Differential-Algebraic Equations. *J. Process Control* **2002**, *12*, 577–585. [CrossRef]
27. Meng, Q.; Xu, J.; Luo, F.; Jin, X.; Xu, L.; Yao, W.; Jin, S. Collaborative and Effective Scheduling of Integrated Energy Systems with Consideration of Carbon Restrictions. *IET Gener. Transm. Distrib.* **2023**, *17*, 4134–4145. [CrossRef]
28. Singh, D.K.; Tirkey, J.V. Valorisation of Hazardous Medical Waste Using Steam Injected Plasma Gasifier: A Parametric Study on the Modelling and Multi-Objective Optimisation by Integrating Aspen plus with RSM. *Environ. Technol.* **2022**, *43*, 4291–4305. [CrossRef]
29. Kaushal, R.; Rohit; Dhaka, A.K. A Comprehensive Review of the Application of Plasma Gasification Technology in Circumventing the Medical Waste in a Post-COVID-19 Scenario. *Biomass Convers. Biorefinery* **2024**, *14*, 1427–1442. [CrossRef]
30. Rosha, P.; Ibrahim, H. Hydrogen Production via Solid Waste Gasification with Subsequent Amine-Based Carbon Dioxide Removal Using Aspen Plus. *Int. J. Hydrogen Energy* **2023**, *48*, 24607–24618. [CrossRef]
31. Rosha, P.; Kumar, S.; Vikram, S.; Ibrahim, H.; Al-Muhtaseb, A.H. H2-Enriched Gaseous Fuel Production via Co-Gasification of an Algae-Plastic Waste Mixture Using Aspen PLUS. *Int. J. Hydrogen Energy* **2022**, *47*, 26294–26302. [CrossRef]
32. Zhou, J.; Ayub, Y.; Shi, T.; Ren, J.; He, C. Sustainable Co-Valorization of Medical Waste and Biomass Waste: Innovative Process Design, Optimization and Assessment. *Energy* **2024**, *288*, 129803. [CrossRef]
33. Kim, D.H.; Park, J.L.; Park, E.J.; Kim, Y.D.; Uhm, S. Dopant Effect of Barium Zirconate-Based Perovskite-Type Catalysts for the Intermediate-Temperature Reverse Water Gas Shift Reaction. *ACS Catal.* **2014**, *4*, 3117–3122. [CrossRef]
34. Fazeli, H.; Panahi, M.; Rafiee, A. Investigating the Potential of Carbon Dioxide Utilization in a Gas-to-Liquids Process with Iron-Based Fischer-Tropsch Catalyst. *J. Nat. Gas Sci. Eng.* **2018**, *52*, 549–558. [CrossRef]

35. Zang, G.; Sun, P.; Delgado, H.E.; Cappello, V.; Ng, C.; Elgowainy, A. The Modeling of the Synfuel Production Process: Process Models of Fischer-Tropsch Production with Electricity and Hydrogen Provided by Various Scales of Nuclear Plants (Program Document). Available online: https://www.osti.gov/biblio/1868524 (accessed on 31 July 2023).
36. Li, K.; Leigh, W.; Feron, P.; Yu, H.; Tade, M. Systematic study of aqueous monoethanolamine (MEA)-based CO_2 capture process: Techno-economic assessment of the MEA process and its improvements. *Appl. Energy* **2016**, *165*, 648–659. [CrossRef]
37. Zhou, J.; Ren, J.; He, C. Turning Sewage Sludge and Medical Waste into Energy: Sustainable Process Synthesis via Surrogate-Based Superstructure Optimization. *Green Chem.* **2025**, *27*, 1777–1788. [CrossRef]
38. Sun, Z.; Zeng, L.; Russell, C.K.; Assabumrungrat, S.; Chen, S.; Duan, L.; Xiang, W.; Gong, J. Solar-Wind-Bio Ecosystem for Biomass Cascade Utilization with Multigeneration of Formic Acid, Hydrogen, and Graphene. *ACS Sustain. Chem. Eng.* **2019**, *7*, 2558–2568. [CrossRef]
39. Paulillo, A.; Sebastiani, A.; Lettieri, P.; Materazzi, M. Decarbonising Waste-to-Energy: A Life Cycle Assessment Study. *Resour. Conserv. Recycl.* **2024**, *209*, 107812. [CrossRef]
40. Solomon, S.; Qin, D.; Manning, M.; Marquis, M.; Averyt, K.; Tignor, M.M.B.; Miller, H.L., Jr.; Chen, Z. Climate Change 2007: The Physical Science Basis. In *Contribution of Working Group II to the Fourth Assessment Report of the Intergovernmental Panel on Climate Change*; Cambridge University Press: Cambridge, MA, USA, 2007; Volume 446, pp. 727–728.
41. Zhou, J.; Ren, J.; He, C. Improved Medical Waste Plasma Gasification Modelling Based on Implicit Knowledge-Guided Interpretable Machine Learning. *Waste Manag.* **2024**, *188*, 48–59. [CrossRef] [PubMed]
42. Minghui, M.; Chuanfeng, Z. Application of Support Vector Machines to a Small-Sample Prediction. *Adv. Pet. Explor. Dev.* **2015**, *10*, 72–75. [CrossRef]
43. Herceg, S.; Ujević Andrijić, Ž.; Bolf, N. Development of Soft Sensors for Isomerization Process Based on Support Vector Machine Regression and Dynamic Polynomial Models. *Chem. Eng. Res. Des.* **2019**, *149*, 95–103. [CrossRef]
44. Alade, I.O.; Zhang, Y.; Xu, X. Modeling and Prediction of Lattice Parameters of Binary Spinel Compounds (AM2X4) Using Support Vector Regression with Bayesian Optimization. *New J. Chem.* **2021**, *45*, 15255–15266. [CrossRef]
45. Schölkopf, B. SVMs—A Practical Consequence of Learning Theory. *IEEE Intell. Syst. Their Appl.* **1998**, *13*, 18–21. [CrossRef]
46. Pisner, D.A.; Schnyer, D.M. *Support Vector Machine. Machine Learning: Methods and Applications to Brain Disorders*; Academic Press: Cambridge, MA, USA, 2020; pp. 101–121. [CrossRef]
47. Understanding Support Vector Machine Regression—MATLAB & Simulink. Available online: https://ch.mathworks.com/help/stats/understanding-support-vector-machine-regression.html (accessed on 7 July 2025).
48. Jain, A.K.; Mao, J.; Mohiuddin, K.M. Artificial Neural Networks: A Tutorial. *Computer* **1996**, *29*, 31–44. [CrossRef]
49. Zhou, J.; Chu, Y.T.; Ren, J.; Shen, W.; He, C. Integrating Machine Learning and Mathematical Programming for Efficient Optimization of Operating Conditions in Organic Rankine Cycle (ORC) Based Combined Systems. *Energy* **2023**, *281*, 128218. [CrossRef]
50. Schulz, E.; Speekenbrink, M.; Krause, A. A Tutorial on Gaussian Process Regression: Modelling, Exploring, and Exploiting Functions. *J. Math. Psychol.* **2018**, *85*, 1–16. [CrossRef]
51. Jäkel, F.; Schölkopf, B.; Wichmann, F.A. A Tutorial on Kernel Methods for Categorization. *J. Math. Psychol.* **2007**, *51*, 343–358. [CrossRef]
52. Rasmussen, C.E.; Williams, C.K.I. *Gaussian Processes for Machine Learning*; Mit Press: Cambridge, MA, USA, 2005. [CrossRef]
53. Neal, R.M. *Bayesian Learning for Neural Networks*; Springer: Berlin/Heidelberg, Germany, 1996; p. 118. [CrossRef]
54. Yang, D.; Zhang, X.; Pan, R.; Wang, Y.; Chen, Z. A Novel Gaussian Process Regression Model for State-of-Health Estimation of Lithium-Ion Battery Using Charging Curve. *J. Power Sources* **2018**, *384*, 387–395. [CrossRef]
55. Chen, T.; Guestrin, C. XGBoost: A Scalable Tree Boosting System. In Proceedings of the ACM SIGKDD International Conference on Knowledge Discovery and Data Mining, San Francisco, CA, USA, 13–17 August 2016; pp. 785–794. [CrossRef]
56. Elavarasan, D.; Vincent, D.R. Reinforced XGBoost Machine Learning Model for Sustainable Intelligent Agrarian Applications. *J. Intell. Fuzzy Syst.* **2020**, *39*, 7605–7620. [CrossRef]
57. Pekel, E. Estimation of Soil Moisture Using Decision Tree Regression. *Theor. Appl. Clim.* **2020**, *139*, 1111–1119. [CrossRef]
58. Zhang, W.; Wu, C.; Tang, L.; Gu, X.; Wang, L. Efficient Time-Variant Reliability Analysis of Bazimen Landslide in the Three Gorges Reservoir Area Using XGBoost and LightGBM Algorithms. *Gondwana Res.* **2023**, *123*, 41–53. [CrossRef]
59. Li, Y.; Jiang, W.; Sun, G. Predicting Environmental Pollution with Gradient Boosting: Application of GBDT Regression Models in Time Series Models. *Lect. Notes Electr. Eng.* **2025**, *1328*, 138–148. [CrossRef]
60. Ma, M.; Zhao, G.; He, B.; Li, Q.; Dong, H.; Wang, S.; Wang, Z. XGBoost-Based Method for Flash Flood Risk Assessment. *J Hydrol.* **2021**, *598*, 126382. [CrossRef]
61. Ullah, Z.; Khan, M.; Naqvi, S.R.; Farooq, W.; Yang, H.; Wang, S.; Vo, D.-V.N. A Comparative Study of Machine Learning Methods for Bio-Oil Yield Prediction—A Genetic Algorithm-Based Features Selection. *Bioresour Technol.* **2021**, *335*, 125292. [CrossRef]
62. Suleman, F.; Dincer, I.; Agelin-Chaab, M. Comparative Impact Assessment Study of Various Hydrogen Production Methods in Terms of Emissions. *Int. J. Hydrogen Energy* **2016**, *41*, 8364–8375. [CrossRef]

63. Heuristic Optimization. *Portfolio Management with Heuristic Optimization*; Springer: Boston, MA, USA, 2005; pp. 38–76. [CrossRef]
64. Lambora, A.; Gupta, K.; Chopra, K. Genetic Algorithm—A Literature Review. In Proceedings of the International Conference on Machine Learning, Big Data, Cloud and Parallel Computing: Trends, Prespectives and Prospects, COMITCon 2019, Faridabad, India, 14–16 February 2019; pp. 380–384. [CrossRef]
65. Zhong, J.; Hu, X.; Zhang, J.; Gu, M. Comparison of Performance between Different Selection Strategies on Simple Genetic Algorithms. In Proceedings of the International Conference on Computational Intelligence for Modelling, Control and Automation, Vienna, Austria, 28–30 November 2005; IEEE: New York, NY, USA; Volume 2, pp. 1115–1120. [CrossRef]
66. Zambrano-Bigiarini, M.; Clerc, M.; Rojas, R. Standard Particle Swarm Optimisation 2011 at CEC-2013: A Baseline for Future PSO Improvements. In Proceedings of the 2013 IEEE Congress on Evolutionary Computation, CEC, Cancun, Mexico, 20–23 June 2013; pp. 2337–2344. [CrossRef]
67. Henderson, D.; Jacobson, S.H.; Johnson, A.W. The Theory and Practice of Simulated Annealing. In *Handbook of Metaheuristics*; Springer: Boston, MA, USA, 2003; pp. 287–319. [CrossRef]
68. Zhang, Z.; Lin, M.; Han, B.; Dai, S. Prediction of Local Scour Depth around Cylindrical Piles: Using Simulated Annealing Algorithm and Ensemble Learning. *Ocean Eng.* **2025**, *330*, 121221. [CrossRef]
69. Zhao, S.; Lu, J.; Yang, J.; Chow, E.; Xi, Y. Efficient Two-Stage Gaussian Process Regression Via Automatic Kernel Search and Subsampling. *arXiv* **2024**, arXiv:2405.13785. [CrossRef]
70. Baziar, M.; Yousefi, M.; Oskoei, V.; Makhdoomi, A.; Abdollahzadeh, R.; Dehghan, A. Machine Learning-Based Prediction of Heating Values in Municipal Solid Waste. *Sci. Rep.* **2025**, *15*, 14589. [CrossRef] [PubMed]
71. Bala, I.; Chauhan, D.; Mitchell, L. Orthogonally Initiated Particle Swarm Optimization with Advanced Mutation for Real-Parameter Optimization. *arXiv* **2024**, arXiv:2405.12542. [CrossRef]
72. Zhou, J.; Ren, J.; He, C. Wind Energy-Driven Medical Waste Treatment with Polygeneration and Carbon Neutrality: Process Design, Advanced Exergy Analysis and Process Optimization. *Process Saf. Environ. Prot.* **2023**, *178*, 342–359. [CrossRef]
73. Lei, Q.; Zhang, S.; Li, Y.; Ding, X.; Wang, Y.; Zheng, L.; Wu, L. Design and Optimization of Poly-Generation System for Municipal Solid Waste Disposal. *J. Clean. Prod.* **2022**, *370*, 133611. [CrossRef]
74. Abhilash; Inamdar, I. Recycling of Plastic Wastes Generated from COVID-19: A Comprehensive Illustration of Type and Properties of Plastics with Remedial Options. *Sci. Total Environ.* **2022**, *838*, 155895. [CrossRef] [PubMed]
75. Wei, Y.; Cui, M.; Ye, Z.; Guo, Q. Environmental Challenges from the Increasing Medical Waste since SARS Outbreak. *J. Clean. Prod.* **2021**, *291*, 125246. [CrossRef]
76. Brillard, A.; Kehrli, D.; Douguet, O.; Gautier, K.; Tschamber, V.; Bueno, M.A.; Brilhac, J.F. Pyrolysis and Combustion of Community Masks: Thermogravimetric Analyses, Characterizations, Gaseous Emissions, and Kinetic Modeling. *Fuel* **2021**, *306*, 121644. [CrossRef]